Accepted Manuscript

Metal endowment reflected in chemical composition of silicates and sulfides of mineralized porphyry copper systems, Urumieh-Dokhtar magmatic arc, Iran

Alireza Zarasvandi, Mohsen Rezaei, Johann G. Raith, Houshang Pourkaseb, Sina Asadi, Madineh Saed, David R. Lentz

Geochimica et Cosmochimica Acta
JOURNAL OF THE GEOCHEMICAL SOCIETY
AND THE METEORITICAL SOCIETY

Metal endowment reflected in chemical composition of silicates and sulfides of mineralized porphyry copper systems, Urumieh-Dokhtar magmatic arc, Iran

Alireza Zarasvandi[*a], Mohsen Rezaei[a] , Johann G. Raith[b], Houshang Pourkaseb[a]
Sina Asadi[c], Madineh Saed[a], David R. Lentz[d]

[a]*Department of Geology, Faculty of Earth Science, Shahid Chamran University of Ahvaz, Ahvaz, Iran*

[b]*Department of Applied Geosciences and Geophysics, Montanuniversität Leoben, Leoben, Austria*

[c]*Department of Earth Sciences, Faculty of Sciences, Shiraz University, Shiraz, Iran*

[d]*Department of Earth Sciences, University of New Brunswick, Fredericton, New Brunswick, Canada*

Abstract

The present work attempts to discriminate between the geochemical features of magmatic-hydrothermal systems involved in the early stages of mineralization in high grade versus low grade porphyry copper systems, using chemical compositions of silicate and sulfide minerals (i.e., plagioclase, biotite, pyrite and chalcopyrite). The data indicate that magmatic plagioclase in all of the porphyry copper systems studied here has high An% and Al content with a significant trend of evolution toward $AlAl_3SiO_8$ and $\square Si_4O_8$ endmembers, providing insight into the high melt water contents of the parental magmas. Comparably, excess Al and An% in the high grade deposits appears to be higher than that of selected low grade deposits, representing a direct link between the amounts of exsolving hydrothermal fluids and the potential of metal endowment in porphyry copper deposits (PCDs). Also, higher Al contents accompanied by elevated An% are linked to the increasing intensity of disruptive alteration (phyllic) in feldspars from the high grade deposits. As calculated from biotite compositions, chloride contents are higher in the exsolving hydrothermal fluids that contributed to the early mineralization stages of highly mineralized porphyry systems. However, as evidenced by scattered and elevated log $(fH_2O)/(fHF)$ and log $(fH_2O)/(fHCl)$ values, chloride contents recorded in biotite could be influenced by post potassic fluids. Geothermometry of biotite associated with the onset of sulfide mineralization indicates that there is a trend of increasing temperature from high grade to low grade porphyry systems. Significantly, this is coupled with a sharp change in copper content of pyrite assemblages precipitated at the early stages of mineralization such that Cu decreased with increasing temperature. Based on EMPA and detailed WDS elemental mapping, trace elements do not exhibit complex compositional zoning or solid solution in the sulfide structure. Nevertheless, significant amounts of Cu and Au are contained in pyrite assemblages as micro- to nano-sized inclusions, especially in the high grade fertile porphyry deposits. However, unexpectedly high concentrations of Te, Se, and Re may be associated with early stage of sulfide

---

[*] Corresponding author. Tel-fax: +98 61333331059;. E-mail address: Zarasvandi_a@scu.ac.ir (A. Zarasvandi).

mineralization, especially when there is no epithermal lithocap. This may highlights the significance of trace metals partitioning in the sulfides formed at the early stages of mineralization in PCDs.

Key words: Silicate chemistry; Sulfides; Porphyry copper systems; Urumieh–Dokhtar Magmatic Arc; Iran

1. Introduction

Porphyry Cu ± Mo ± Au mineralization forms in magmatic - hydrothermal systems following the shallow emplacement (5 to 15 km depth) of metal-rich oxidized magma saturated with H_2O, S, and Cl (Sillitoe, 2010; Richards, 2011). The deposits are usually centered on volumetrically small cupolas on the top of subjacent larger, batholith-sized intrusions (Hedenquist and Lowenstern, 1994; Sillitoe, 2010). Most porphyry deposits are found above former to active subduction zones in association with subduction-related, calc-alkaline silicic magmas (Richards, 2003; Sillitoe, 2010; Sun et al., 2013). However, it is now recognized that these deposits may also form in collisional settings (e.g., Chen et al., 2015; Richards, 2015a, b). Examples of the latter are the Miocene porphyry Cu–Mo deposits in Gangdese belt on the south Tibetan Plateau (e.g., Hou et al., 2009; Wang et al., 2014a,b), the Eocene Yulong porphyry Cu belt (Liang et al., 2006), and arguable occurrences in Pakistan and Iran (Richards et al., 2012; Asadi et al., 2014).

The Cenozoic Urumieh-Dokhtar magmatic arc (UDMA) in Iran is considered as one of the major Cu-bearing belts with high potential for the occurrence of economic world class giant to sub-economic small porphyry Cu ± Mo ± Au mineralization (e.g., Shafiei et al., 2009; Richards et al., 2012; Asadi et al., 2014; Zarasvandi et al., 2013, 2015a; Fig. 1; Table 1). In this belt, high Sr/Y magmas responsible for Cu-mineralization are strictly restricted to the late- stage Miocene magmatism, forming approximately 29 m.y. after the initiation of magmatism along the UDMA (Richards, 2012; Aghazadeh et al., 2015; Zarasvandi et al., 2015a). It is thought that subduction modified juvenile lower arc crust that inherited its arc signature with respect to F, Cl, and Cu is the source of fertile magmatism capable of producing porphyry mineralization in UDMA (Asadi et al., 2014; Zarasvandi et al., 2015b).

Presently, the chemical compositions of silicates and sulfides are commonly used to decipher the physico-chemical attributes of the magmatic – hydrothermal stages of porphyry systems. For example, Williamson et al. (2016) provided a link between major and trace element composition of magmatic plagioclase and magmatic processes operating in barren and fertile porphyry copper systems worldwide. Biotite, a common phase in porphyry systems, has long been recognized to record the physico-chemical conditions (i.e., oxidation states, halogen fugacity and temperature) of the magmatic to hydrothermal stage (e.g., Beane, 1978; Munoz, 1992; Selby and Nesbitt, 2000; Mercer and Reed, 2013). Aside from silicate chemistry, the geochemical features of sulfide mineralization were introduced as new tools in monitoring the hydrothermal fluid evolution in porphyry systems. Recently, detailed EMPA and WDS mapping of pyrite

assemblages in Dexing porphyry Cu deposit highlighted the significant role of pyrite in metal partitioning and speciation during evolution of porphyry Cu mineralization (Reich et al., 2013a); changes in the composition of hydrothermal fluids are reflected in the trace element contents of pyrite. Using the chemical variation of pyrite as a tool for interpreting hydrothermal fluid evolution has also been extended from porphyry to epithermal deposits (e.g., Maydagan et al., 2013; Franchini et al., 2015).

Taken as a whole, there are many geological and geochemical variables that may have effect on the evolutionary path of a given porphyry system toward being an economic deposit. For example, comparing the magmatic-hydrothermal features of barren and mineralized intrusions has revealed that magmatic history and petrogenesis evolution (e.g., Richards et al., 2012; Wang et al., 2014a,b), as well as composition and evolution of exsolving hydrothermal fluids (e.g., Audetat et al., 2008) may have decisive role in the mineralization potential of porphyry intrusions. Moreover, assessments of world class giant porphyry deposits have shown that giant porphyry deposits may occur when there are optimum coincidence of non-unique geological factors i.e., distinct tectonic configurations, focused fluid flow, and reactive host rocks (Richards, 2013).

Aside from being a supergiant or barren porphyry system, the fact is that the porphyry copper systems generally exhibit a spectrum of mineralization from low-grade sub-economic to high-grade economic ore systems. Although there are many variables that could affect metal deposition and enrichment in porphyry Cu systems, recent findings suggest that silicate and sulfide chemistry could be linked directly to the physicochemical attributes of primary metal deposition in the porphyry copper systems (e.g., Williamson et al., 2016; Reich et al., 2013a). Accordingly, in this paper we provide a comprehensive geochemical data set on the silicates (plagioclase, biotite), and sulfides (pyrite, chalcopyrite) coupled with WDS elemental mapping for a number of Miocene high grade and low grade porphyry copper deposits in the UDMA (Fig. 1; Table 1). The data are used to discriminate and characterize physicochemical parameters (e.g., temperature, H_2O content, halogen fugacity, and Cu budget) that prevailed during magmatic and early stages of mineralization in PCDs having variable degrees of mineralization.

2. Methodology
2.1. Sampling strategy

Porphyry copper systems located in the south eastern (Meiduk, Sarkuh, Iju, Keder, and Chahfiruzeh), and central (Dalli) parts of the UDMA were involved in the present work (Fig. 1; Table 1). Before the field campaign and sampling, the characteristics and spatial distributions of alteration assemblages in and around the selected porphyry copper deposits were constrained from assay data, and drill core logging (see supplemental file). In these deposits, the intrusions have a range of rock compositions. In order to minimize possible differences related to rock

compositions, the selected deposits were divided into two major groups: quartz diorite and granodiorite. The quartz diorite group includes the Dalli and Chahfiruzeh as examples of relative high grade porphyries, and Keder as a low grade porphyry system. The second group contains the large economic Meiduk deposit and two low grade deposits Sarkuh and Iju. In order to avoid effects of alteration on the composition of plagioclase, plagioclase samples without obvious petrographic evidence for alteration were selected. In all of these porphyry copper systems, the bulk of Cu-sulfide mineralization generally occurs at the waning stages of potassic alteration. Accordingly, for characterizing the geochemical attributes of primary sulfide mineralization in high grade and low-grade porphyry copper systems, biotite, pyrite and chalcopyrite were taken from the potassic zones of the systems. All selected biotite samples are spatially associated with pyrite and chalcopyrite and are interpreted to represent hydrothermal biotite formed or re-equilibrated during potassic alteration.

2.2. Analytical methods

The chemical compositions of biotite, plagioclase, pyrite and chalcopyrite were analyzed on carbon coated polished thin sections using a wave length dispersive electron probe microanalyzer (EPMA) (Tables 2 to 5, and supplementary Tables 2-5). All samples were prepared and analyzed in the Eugen F. Stumpfl Laboratory of Montanuniversität Leoben, Austria using a Superprobe Jeol JXA 8200 instrument. The same instrument was used for obtaining the back-scattered electron images. Analyses were done at accelerating voltage of 15 kV with a beam current of 10 nA and beam size of about 1 μm. The counting time was between 20 and 100 s. For analyzing the silicates, the calibration standards were natural adularia, atacamite, rhodonite, titanite, fluorite, labradorite, wollastonite, and olivine for F, Si, Al, Fe, Mg, Ti, Cl, Ba, and Mn. The detection limits (in wt.%) as calculated by the instrument software for each element include: 0.25 for F, 0.02 for Na, 0.01 for Mg, Al, Si, Ca, K, and Cl, and 0.03 for Ti, Fe, and Mn. For the EMP data, FeO represents total Fe calculated as FeO. For sulfide analyses the calibration standards used were pyrite for Fe and S, chalcopyrite for Cu, pentlandite for Ni, $AuTe_2$ for Au and Te, Bi_2Se_3 for Se, $CoAs_3$ for Co, GaAs for As, $AgBiSe_2$ for Ag, and ZnS for Zn. Moreover, for the sulfides elemental maps were obtained using wavelength-dispersive spectrometry (WDS) X-ray mapping capability of the electron probe microanalyzer. Elemental mapping analyses were performed at accelerating voltage of 20 kV, beam current of 50 nA beam, spot size of 1μm and counting time of 30 ms/step. More details on the EPMA analyzing procedure in the Eugen F. Stumpfl Laboratory are explained in Reich et al. (2013a).

3. Results

3.1. Composition of plagioclase

Here we present geochemical data on the magmatic plagioclase in the high grade Meiduk and Dalli porphyries and the Iju, Sarkuh, and Keder low grade ones. Meiduk, Iju and Sarkuh

represent the granodiorite group, while Dalli and Keder belong to the quartz diorite group. Representative electron microprobe analyses of plagioclase are given in Table 2. Plagioclases from both groups show a wide compositional range. In the granodiorite porphyries, plagioclase has SiO_2 values between 47.89-63.29 wt.% with Al_2O_3 of 23.33-33.11 wt.% and CaO of 4.73-15.85 wt.%. The K_2O and Na_2O concentrations are between 0.069-0.715 and 2.07-8.57 wt.%, respectively. The plagioclase from quartz diorite porphyries contains 55.7-71.02 wt.% SiO_2, and 19.49-28.51 wt.% Al_2O_3 with CaO of 0.02-10.11 wt.%. The K_2O and Na_2O ranges from 0.26-1.22 wt.% and 3.97-11.70 wt.%, respectively. In order to check whether plagioclase has been substantially modified by the alteration processes that are common in porphyry systems, the data were plotted in the SiO_2 vs. $CaO + Na_2O + K_2O$ diagram (Fig. 2). In this diagram, except for two samples of Keder, almost all of samples fall along the tie line between albite and anorthite, which rules out effects of alteration on the primary major element compositions of plagioclase in these samples.

3.2. Composition of biotite
3.2.1. Biotite elemental systematics

In order to decipher the physicochemical attributes of the hydrothermal system during the early stages of sulfide mineralization in the high grade and low grade deposits, biotite selected from the potassic alteration zone was analyzed. Representative electron microprobe analyses are listed in Table 3. Mineral formulae were calculated based on 22 oxygens. Despite the range of whole rock compositions, most biotite analyses plot in the Mg biotite field (Fig. 3A). Only biotite from the low grade Keder deposit extends into the phlogopite field (Fig. 3A). In the $(FeO+MnO)$ - MgO -TiO_2 diagram, biotite analyses plot near to the boundary of primary and re-equilibrated biotite fields (Fig. 3B), confirming that biotite formed in equilibrium with the magmatic - hydrothermal fluids in porphyry system (e.g., Boomeri et al., 2009).

The contents of Na, Ti, and XFe (=Fe/Fe+Mg) of biotite (atoms per formula unit (*apfu*)) are listed in Table 3, (see also supplementary Table 3), and illustrated in Fig. 4. The re-equilibrated biotites from the potassic alteration zone at Mediuk deposit display the lowest level of Na (*apfu*), whereas all the others are higher. There is a gradual change of Na in biotite from high grade to low grade porphyries in both the quartz diorite and granodiorite groups. In the granodiorite group, Na *(apfu)* increases from Meiduk, to the Iju and Sarkuh. In the quartz diorite group Na tends to be more variable and higher in the Keder low grade deposit (Fig. 4). Sodium content of biotite can be linked with composition of plagioclase in the deposits. Albite endmember in plagioclase reaches the highest values in Keder and Iju deposits (average 93.4 and 68.7 Ab%, respectively; Table 2, and supplementary Table 2), while it is lowest at Meiduk (average 42.5 Ab%). The Ti content *(apfu)* of biotite shows marked differences between high grade and low grade porphyries of the granodiorite group (Fig. 4) but not in the quartz diorite porphyries. The Fe/(Fe + Mg) values of biotite are compared in Fig. 4. Again, biotite from Meiduk shows the largest variation. Also, there is a tendency of decreasing Fe/(Fe + Mg) between high grade and low grade porphyry copper systems in the quartz diorite group (Fig. 4).

5

3.2.2. Biotite halogen content

The concentrations of Cl and F in biotite samples are listed in Table 3, and supplementary Table 3. X_F (=F/F+Cl+OH) values in biotites are highly variable, ranging on average from 0.01 X_F in Meiduk to Sarkuh (average 0.06), Chahfiruzeh (average 0.09), Dalli (average 0.12), Iju (average 0.17), and Keder (average 0.29). The X_F values show a distinct trend of increasing from high grade to low grade porphyries in both the quartz diorite and granodiorite groups (Fig. 5). In contrast, the variation in chlorine is limited. The average X_{Cl} values are: Meiduk (0.007), Keder (0.009), Iju (0.013), Sarkuh (0.015), Dalli and Chahfiruzeh (0.02). Also, X_{Cl} values represent two trends of increasing and decreasing from high grade to low grade porphyry copper systems of the granodiorite and quartz diorite series, respectively (Fig. 5).

3.3. Composition of sulfides

The chemical compositions of pyrite and chalcopyrite occurring as fine-grained disseminations and early sulfide veins related to potassic alteration are given in Tables 4 and 5, and supplementary Tables 4 and 5. Pyrite and chalcopyrite contain a wide range of trace elements, the most abundant being As, Te, Co, Au and Mo. In all of the studied deposits, the elemental concentrations for major components are relatively homogenous, so that the overall compositions of pyrite (Fe: 45.16 – 47.03, average 46.36; S: 50.76 – 53.73, average 52.18 wt. %) and chalcopyrite (Fe: 29.63- 31.06, average 30.16; S: 29.83- 35.50, average 34.38; Cu: 32.87 – 36.49 average 34.06 wt. %) are analogous to those reported previously for other porphyry copper systems (e.g., Dexing porphyry Cu deposit, China; Reich et al., 2013a; Altar porphyry Cu-Au deposit, Argentina; Maydagan et al., 2013; Agua Rica porphyry Cu-Mo deposit, Argentina; Franchini et al., 2015).

Copper, Au and Mo are considered as the main commodities in porphyry-style ores. In the early stage of sulfide mineralization, the Cu contents of pyrite in granodiorite porphyries including Meiduk, Iju, and Sarkuh (average 0.137 wt. %) are higher than those of quartz diorite porphyries (Dalli, Chahfiruzeh and Keder; average 0.011 wt. %). Also, the highest Cu contents of pyrites are in the high grade porphyries, i.e., Meiduk (average 0.26 wt. %), Dalli (average 0.024 wt. %), and Chahfiruzeh (average 0.0011 wt. %). On the contrary, pyrite compositions in low grade deposits are characterized by lower Cu contents (Sarkuh 0.007 wt. %; Iju 0.010 wt. %, and Keder below detection (b.d.). Based on the EPMA data, the concentrations of Cu in the chalcopyrite samples of granodiorite porphyries (average 34.26 wt. %) are slightly greater than in the quartz diorite porphyries (33.91 wt. %). Aside from Cu, significant Au contents were also found in the pyrite and chalcopyrite samples associated with early stage of sulfide mineralization. Spot analyses conducted on the pyrite indicate that Au content varies from <0.006 to 0.046 wt. % (average 0.0162 wt. %), which is significantly greater than that of chalcopyrite samples (<0.001 to 0.043 wt. %; average 0.0081 wt. %). In the early stages of sulfide mineralization, there are no significant differences between Au contents of pyrite in granodiorite (average 0.0162 wt. %), and quartz diorite (average 0.0161 wt. %) porphyries. Such characteristics are also observed in

chalcopyrite compositions, where Au contents (on average) in chalcopyrite samples of granodiorite deposits are analogous to those of quartz diorite porphyries (0.0073 and 0.0087 wt. %, respectively). Similarly, the Mo contents of pyrite (average 0.6963 wt. %) are slightly higher than those of chalcopyrite (average 0.4950 wt. %). The Mo contents of pyrite in granodiorite (average 0.697 wt. %) and quartz diorite (average 0.695 wt. %) porphyries are relatively constant.

4. Discussion

4.1. Fertile magmatic systems associated with porphyry Cu mineralization in UDMA

A recent overview on the origin of the mineralized porphyry intrusions in the UDMA is provided by Shafiei et al. (2009), and Asadi et al. (2014). They specified a model comprising partial melting of thickened mafic lower crustal rocks for the generation of hydrous, relatively oxidized calc-alkaline magmas with the high potential to form porphyry Cu ± Mo ± Au systems. This model invokes a temporal evolution from early pre-collisional Eocene–Oligocene intrusions to late-stage Miocene (and younger) adakite-like mineralized intrusions (e.g., Sarcheshmeh, Meiduk, Abdar, Iju, Chahfiruzeh, Sarkuh and Keder). As depicted in Richards et al. (2012) and Zarasvandi et al. (2015a) the temporal evolution in the porphyry copper systems of the UDMA is coeval with a progression toward higher magmatic water contents of late stage Miocene mineralized porphyries compared to those of early pre-collisional porphyry intrusions. In other words, the normal andesitic calc-alkaline signatures for the early magmatic products evolved toward an adakite-like calc-alkaline character for the younger intrusions. Accordingly, a trend of arc maturation and evolution of the magmatic system over a period of time has been traced in UDMA (see Richards et al., 2012; Zarasvandi et al., 2015a). Importantly, this evolution has been detected in some other porphyry copper belts worldwide; e.g., Metaliferi Mountains, Romania (e.g., Roşu et al., 2004), and porphyry Cu ± Mo ± Au systems in the eastern Gangdese magmatic belt in southern Tibet (e.g., Wang et al. 2014a, b). A recent study by Zarasvandi et al. (2015b) indicates that such a geochemical evolution is not only observed on the large scale of magmatic belts containing porphyry deposits (especially those located along the Neo-Tethyan arc systems i.e., UDMA in Iran, Chagai volcano-plutonic belt in Pakistan, and Gangdese belt in Tibet) but is also developed in individual porphyry deposits. For example, porphyry intrusions in the Dalli deposit are characterized by a trend of transition from normal andesitic calc-alkaline to adakite-like high-K-calc-alkaline magmas. This is coupled with other geochemical changes i.e., strong decreases of Y with increasing SiO_2 content (Y and MREE are preferentially partitioned in hornblende during the magmatic evolution; e.g., Davidson et al., 2007), and increasing of Eu/Eu* with increasing SiO_2 values (Zarasvandi et al., 2015b). Such features as formerly delineated in a regional scale (e.g., Richards et al., 2012; Zarasvandi et al., 2015a), are consistent with formation of later high Sr/Y hydrous magmas and support fractional crystallization of amphibole as being responsible for the adakite-like geochemical character of mineralized porphyry intrusions.

4.2. Plagioclase composition linked to magmatic processes

Water-rich magmas with high Sr/Y ratios apparently have a high potential to form fertile porphyry intrusions. Based on recent findings, subtle changes in the water contents of porphyry magmas could be reflectd by the major element composition of plagioclase (e.g., Ushioda et al., 2014; Williamson et al., 2016; Richards, 2016). According to Williamson et al. (2016) aluminium contents of plagioclase in the fertile I-type, medium (to low) K calc-alkaline rocks appear to be higher than those of barren ones (Fig. 6). In the Al / (Ca + Na + K) (*apfu*) vs. An% discrimination plot (Fig. 6), the high grade and low grade porphyry deposits of UDMA plot collectively in the field of calc-alkaline rocks associated with PCDs; i.e. they are characterized by excess Al. The plagioclase samples display a negative correlation between Al + Si (*a.p.f.u.*) and Ca + Na + K (*a.p.f.u.*) (Fig. 7), however the negative correlation in the Meiduk large economic deposit is stronger than that of other deposits. This feature suggests that excess Al may be contained within large cation (M) sites by substitution of Al for Ca and Na in the plagioclase structure (Fig. 7; Williamson et al., 2016). It is evident that plagioclase compositions in high grade and low grade porphyries show $AlAl_3SiO_8$ and $\square Si_4O_8$ substitution; $\square$ refers to defect on the M site, leading to a large vacancy in the M-site and subsequent incorporation of H_2O molecules in feldspar structure (see Kyono and Kimata, 2001). The incorporation of excess Al and vacancies via the $AlAl_3SiO_8$ and $\square Si_4O_8$ substitution schemes maybe due to the elevated PH_2O (partial pressure of water) in the porphyry associated intrusions (c.f. Williamson et al. 2016).

The anorthite component (An%) is higher in the granodiorite porphyries (Meiduk, Sarkuh and Iju) than in the quartz diorite porphyries (Fig. 8). Importantly, it reaches the highest values in the highly economic Meiduk deposit. Overall, selected porphyry copper systems exhibit a gradual decrease in An% from high grade to low grade porphyries grouped in granodiorite and quartz diorite (Fig. 8). Naturally, in the plagioclase structure An% increases linearly with increasing alumina contents (not shown). On the other hand, the experimental data of Hattori and Sato (1996), and Ushioda et al. (2014) indicated that the An% of plagioclase could be a function of variation in the H_2O content of silicate magma, so that with more water, higher An contents are produced. Taken as a whole, it is evident that variation in magmatic water as coupled with alumina content and An% could be considered as a key factor for discriminating barren from fertile porphyry intrusions, and also could be linked to the mineralization potential of porphyry intrusions.

4.2.1. Plagioclase composition: implications for hydrothermal alteration intensity

In porphyry copper systems, declining temperature of the hydrothermal fluids destabilise feldspars in the presence of H^+, OH^-, K, and S that leads to the occurrence of feldspar-destructive alteration (phyllic) (Pirajno, 2009; Sillitoe, 2010). Although it has been long recognized that phyllic alteration in porphyry copper systems forms as the result of mixing between meteoric and magmatic fluids, some studies have indicated that feldspar-destructive alteration may occur by

high-temperature saline magmatic fluids (e.g., Harris and Golding, 2002). In addition to the composition and proportion of meteoric and/or magmatic fluids, the chemical composition of feldspars seems to have a role in the occurrence and/or expansion of feldspar-destructive alteration. However, such relation has not yet been delineated in porphyry copper systems.

Based on assay data and drill core logs, the low grade Keder deposit having the lowest Cu contents (Table 1), exhibits the lowest degree of feldspar-destructive alteration (Appendix A.2.6). In contrast, a relatively distinct and significant phyllic alteration occurs in the economic Meiduk deposit. Experimental studies have revealed that K-feldspar has a slower dissolution rate than Na-feldspars under acidic pH conditions in spite of their identical Al contents (e.g., Harouiya and Oelkers, 2004). Nevertheless, at acidic pH conditions the dissolution rate would increase in the plagioclase solid solution series with increasing Al content (Stillings et al., 1996). Preferential leaching of Al is the main reason for the higher dissolution rate of Ca-rich feldspars compared to Na and K-rich feldspars (e.g., Zhang and Luttge, 2009). Generally, in the plagioclase solid solution series, the Al content increases linearly from the Na-endmember albite ($Na[AlSi_3O_8]$) to the Ca-endmember anorthite ($Ca[Al_2Si_2O_8]$) (Zhang and Luttge, 2009). As shown in the Figure 8, samples of the Keder low grade deposit are characterized by the lowest amount of An % (and subsequent lowest Al content), while the Meiduk large economic deposit contains the highest An% content. Overall it seems that excess Al in the plagioclase structure accompanied by high magmatic water contents could also be considered as a critical parameter for enhancing feldspar-destructive alteration during the hydrothermal evolution of porphyry copper systems.

4.3. Temperature at the onset of sulfide mineralization

Two geothermometers have previously been used to estimate temperatures of hydrothermal biotite associated with potassic alteration in porphyry copper systems: The Henry et al. (2005) (e.g., Mercer and Reed, 2013; Parsapoor et al., 2015; Maydagan et al., 2016), and the Beane (1978) biotite geothermometers (e.g., Ayati et al., 2008; Afshooni et al., 2013). The Henry et al. (2005) biotite geothermometer was originally proposed for graphitic, peraluminous metapelites containing rutile or ilmenite and that equilibrated at roughly 4-6 kbar. This thermometer is based on the T-dependence of Ti substitution in biotite. According to Robert (1976), and Henry et al. (2005), the solubility of Ti in Mg-biotite is a function of temperature and pressure. Titanium substitution in the octahedral sites of Mg-biotite increases with increasing temperature but decreases with increasing pressure. Also, the temperature dependence of Ti substitution in biotite is controlled by presence of Fe-Ti oxides for buffering TiO_2 chemical potential (e.g., Mercer and Reed, 2013). The calibration range specified for Henry et al. (2005) geothermometer is X_{Mg} = 0.275–1.000, Ti = 0.04– 0.60 apfu, T = 480–800 °C, and P = 400–600 MPa. The precision of this geothermometer is ±24°C for temperatures between 480° to 700°C and ±12°C for 700° to 800°C. Mercer and Reed (2013) have pointed out that application of this thermometer to rocks from

porphyry systems requires evaluation of whether chemical equilibrium has been attained and preserved.

The Beane (1978) biotite geothermometer, which was primarily applied to hydrothermal biotite from the potassic alteration zone in North American porphyry copper deposits, uses the composition of biotite coexisting with common minerals of potassic alteration including magnetite and K-feldspar. This method is based on the evaluation of mixing parameters for the Mg^{2+} - Fe^{2+} - Fe^{3+} substitution in biotite (Beane, 1978). As estimated from the X_{phl} and XPDoxy (Fe^{3+}/sum of octahedral ions) of hydrothermal biotite (Beane, 1974). The Henry (2005) thermometer seems less applicable to our samples. The recommended pressure range of 400–600 MPa is higher than pressures in the potassic alteration zone of porphyry copper systems (<250 Mpa; Rezaei, 2017). Also, ilmenite and/or rutile that are required for buffering the chemical potential of TiO_2 are not common minerals in the potassic alteration zones of the studied porphyry copper systems. Therefore, we have used the Beane (1978) geothermometer for estimating the temperature of potassic alteration in the porphyry copper systems studied here (Table 3, and supplementary Table 3). Overall, temperatures of potassic alteration in quartz diorite porphyry systems appear to be higher than those of the granodiorite group (Fig. 9). Also high grade porphyry copper systems are characterized by lower temperatures compared to those of the low grade deposits (Fig. 9). Given that analyzed biotite samples are spatially associated with early sulfide mineralization and potassic alteration, such temperatures could reflect the onset of sulfide mineralization in both high grade and low grade porphyry copper systems.

4.4. Halogen fugacities of fluids

Halogens such as chloride and fluoride are important for many magmatic and hydrothermal processes, most notably, transporting of metals in melts and hydrothermal fluids in porphyry copper systems (Richards, 2011). Because of the similar ionic radii of F^- (1.33 Å; Shannon, 1976) and OH^- (1.32–1.37 Å), F^- is much more easily incorporated into the hydroxyl site of biotite than the larger Cl^- (1.81 Å). Accordingly, F^- is less incompatible than Cl^- in melt-fluid systems (Teiber et al., 2015). The evidence of such characteristic can be seen in the distinct negative correlations between molar fractions of fluoride ($XF = F / (F + Cl + OH)$) and hydroxyl (not shown), while Cl^- displays no significant variation with hydroxyl content. A quantitative approach for extracting the relative HF and HCl fugacities based on Cl and F contents in biotites of either magmatic or hydrothermal systems has been described by Munoz (1992) (Equations 1–3). Equations 1-3 are based on revised coefficients for F – Cl – OH partitioning between biotite and the hydrothermal fluid (Zhu and Sverjensky, 1991, 1992).

$$\text{Log } (f\text{H}_2\text{O}/f\text{HF})^{fluid} = 1000/T\left(2.37 + 1.1X_{Mg}\right) + 0.43 - \log \left(\frac{X_F}{X_{OH}}\right)^{biotite} \tag{1}$$

$$\text{Log } (f\text{H}_2\text{O}/f\text{HCl})^{fluid} = 1000/T\left(1.15 + 0.55X_{Mg}\right) + 0.68 - \log \left(\frac{X_{Cl}}{X_{OH}}\right)^{biotite} \tag{2}$$

$$\text{Log } (f\text{HF}/f\text{HCl})^{fluid} = -1000/T\big(1.22 + 1.65X_{Mg}\big) + 0.25 + \log \big(\frac{X_F}{X_{Cl}}\big)^{biotite} \qquad (3)$$

Here, X_F, X_{Cl}, and X_{OH} refer to the mole fractions of F, Cl, and OH in the hydroxyl site of biotite, respectively. X_{Mg} is the sum of Mg/sum octahedral cations, and T is the equilibrium temperature (in Kelvin) of the halogen exchange. The calculated log $f\text{H}_2\text{O}/f\text{HF}$, log $f\text{H}_2\text{O}/f\text{HCl}$, and log $f\text{HF}/f\text{HCl}$ ratios are given in Table 3 and shown on Figure 10. It is evident that fluids of all porphyry copper systems are relatively water-rich owing to more than 3 orders of enrichment relative to halogen fugacity (Table 3, and supplementary Table 3). Generally, the halogen vs. X_{Fe} / X_{Mg} plots of biotites formed in equilibrium with a homogenous fluid under the same T, P, and fluid compositions would result in linear trends parallel to the slopes of the lines of equal log fugacity ratios (Zhu and Sverjensky, 1992; Fig. 10), which is not the case. This might be explained by coupled variations in $f\text{O}_2$, $f\text{S}_2$ and halogen concentrations of the fluids and fluid - wall rock interactions (e.g., Selby and Nesbitt 2000, Boomeri, 2010). Moreover, as depicted in Zhang et al. (2016) continuous equilibration of biotite with fluids over a range of temperatures and fluid composition might also explain the scattering in log X_F/X_{OH} vs. X_{Fe} and log X_{Cl}/X_{OH} vs. X_{Mg} plots. As seen on Fig. 10, biotites of Meiduk have a much larger X_{Mg} range compared to the other deposits. This might be due to variable sulfur (and oxygen) activity of the fluid, which affected the Fe availability through the variable aqueous sulfide activity. This in turn may have affected the Fe availability through variable precipitation of magnetite, pyrite, and chalcopyrite within potassic alteration and/or incorporation of different amounts of F (Munoz and Ludington, 1974; Grew et al., 2006; Mercer and Reed, 2013). The latter is confirmed by broad range of F contents in the Meiduk samples (Fig. 5a).

A comparison between fugacity ratios of hydrothermal fluids in the studied porphyry copper systems and other porphyry Cu systems is shown in Fig. 11. It is evident that the hydrothermal fluids of Meiduk deposit have the high and scattered log $f\text{H}_2\text{O}/f\text{HF}$ and log $f\text{H}_2\text{O}/f\text{HCl}$ values. These values are similar to higher than those determined for Sarcheshmeh and Bingham (Fig. 11). As explained in Selby and Nesbitt (2000) the spread in the fugacity ratios may indicate the modification of biotite halogen chemistry by post-potassic hydrothermal fluids.

4.5. Trace element distribution in early sulfide mineralization: solid solution vs. mineral inclusions

Our data indicate that the early sulfide mineralization associated with potassic alteration is characterized by a wide range of trace element concentrations, even in the same sample. It should be noted that this is a common geochemical feature in hydrothermal sulfides, as reported in other porphyry deposits (see Reich et al., 2013a; Cioacă et al., 2014). The simplest explanation for such heterogeneities appears to be the occurrence of complex compositional zoning (e.g., Reich et al., 2013a) or micro- to nano-sized inclusions/particles, and the grain-scale

heterogeneous distribution of elements (e.g., Reich et al., 2005; Cioacă et al., 2014). For example, a broad correspondence of Au with As has been detected in pyrite samples of some porphyry copper systems. It is thought that the contribution of gold (as Au^{1+}) in the pyrite structure is strictly related to its As content, which replaces sulfur (Palenik et al., 2004; Reich et al., 2005; Cioacă et al., 2014). Accordingly, Reich et al. (2005) introduced a discrimination line between the occurrence of Au as solid solution and nanoparticles in the diagram of Au solubility as a function of As content (Fig. 12); based on the various experimental evidence, below this line Au would be present as solid solution (Au^{1-}), while above it a significant amount of Au is contained as nano-sized particles of native Au (probably Au^0 or Au-tellurides.) (Fig. 12; Reich et al., 2005). Most of our samples from both the high grade and low grade deposits plot in the field of pyrite with Au inclusions, similar to Au contents of pyrites in the Colnic and Rovina porphyry deposits, Romania (Fig. 12). It seems that heterogeneous occurrence of ppm levels of Au as high as ~460 ppm is most likely related to presence of micro- to nano-sized inclusions/particles in the pyrite samples of high grade and low grade deposits. In contrast to pyrite samples in Dexing porphyry deposit (Fig. 12), in which Au exhibits a distinct correlation with As (Reich et al., 2013a), our data indicate that except for some deposits (i.e., Iju porphyry), Au does not vary significantly with As content (Fig. 13). The imperfect covariation of Au with As highlights the role of nano-sized Au particle inclusions in heterogeneous and independent distribution of Au in the pyrite samples (Franchini et al., 2015; Fig. 13).

In order to substantiate the presence of complex compositional zoning and verify whether a particular trace element occurs as a homogeneous substituent or as micro- to nano-sized inclusions, relative abundances of trace elements within pyrite and chalcopyrite samples based on back-scattered electron (BSE) images and wavelength-dispersive spectrometry (WDS) X-ray elemental maps of some representative samples has been evaluated (Figs. 14 and 15).

Among all the analyzed pyrites, the highest concentrations of Cu were detected in the Meiduk samples. Copper reaches up to 1.36 wt. % in the some Meiduk pyrite samples (Table 4). The Cu concentrations in excess of ~10,000 ppm (~1 wt. %) is attributed to local enrichment, possibly due to the presence of aggregates of micro- to nano-sized inclusions/particles of chalcopyrite or other Cu-bearing sulfide minerals (Reich et al., 2013a; Franchini et al., 2015). Detailed back-scattered electron (BSE) images coupled with (WDS) X-ray elemental maps of pyrite associated with early stage of mineralization in the potassic alteration of Meiduk deposit reveal that the extremely high concentration of Cu in pyrite at Meiduk appear to be related to the presence of chalcopyrite micro-inclusions (Figs. 14A and B). Importantly, such features are not observed within any of the pyrite samples from low grade deposits (e.g., Keder porphyry; Fig. 15). In the WDS elemental maps, the relative enrichment of Mo in the pyrite (light blue), contrasts with low Mo contents in chalcopyrite (dark-blue) (Figs. 14E and 15F). Except for some limited and local Ni enrichments in pyrite (e.g., Meiduk; Fig. 14D), Ni is preferentially concentrated in the chalcopyrite as evidenced by greenish-blue areas, contrasting with light-blue areas in pyrite maps

(Figs. 14D and 15E). The major components of chalcopyrite and pyrite, including Cu, Fe, and S have a homogenous distribution pattern in all of the elemental maps (Figs. 14B, C and 15B, C).

4.5.1. Trace metals in sulfides: Economic importance?

The EMP analyses conducted on chalcopyrite and pyrite revealed detectable concentrations of Pb, Zn, Te, Re, and Ag contained mostly in chalcopyrite, while pyrite may contain higher concentrations of Mo, Co, As and Au. Most of the pyrite and chalcopyrite samples are characterized by relatively high Te contents (pyrite, up to 178 ppm; chalcopyrite, up to 192 ppm), which is above the 1.5–3 ppm threshold for economic extraction as a by-product from Cu processing (Ayres et al., 2002; Cioacă et al., 2014). Bornite and chalcopyrite are considered as the main Ag carriers in hydrothermal sulfide ores (Cook et al., 2011; Reich et al., 2013b). Our data indicate that are a wide ranges of Ag concentrations (pyrite: b.d. to 70 ppm; chalcopyrite: b.d. to 200 ppm) which are higher than the average bulk ore grade of Ag (1.7 ppm) reported for porphyry Cu-Au deposits (Cox and Singer, 1988). Previous researches have indicated that the enrichments of Au, Ag and Te are common in epithermal systems (Cook and Ciobanu, 2004; Popescu et al., 2013). Recent work on sulfides from porphyry copper deposits in Metaliferi Mountains (Cioacă et al., 2014), however, indicates that Au, Ag, and Te may also be enriched in porphyry-type mineralization. Selenium is only detectable in some pyrite samples (up to 127 ppm). Importantly, these values are higher than those specified to be an economic by-product of Cu extraction (4 ppm Se; Cioacă et al., 2014). In porphyry copper systems, Re is commonly concentrated within the molybdenite. Despite of the heterogeneous distribution of Re (pyrite: <9 to 230 ppm; chalcopyrite: <10 to 500 ppm), the erratic and anomalously high Re content (up to 500 ppm in Dalli PCD) in some chalcopyrite samples indicates that further studies are necessary to better evaluate the economic potential of Re in porphyry copper systems of UDMA. Our data suggest that pyrite and chalcopyrite in Iranian porphyry copper deposits seem to be more important than previously thought for scavenging economic valuable trace elements such as Re.

### 4.6. Combining silicate and sulfide geochemistry: Implications for metal fertility in PCDs

Considering the magmatic stage, it is evident that variations in the H_2O contents of silicate magmas (traced by An% and Al content of plagioclase) could be linked directly to the mineralization potential of mineralized porphyry intrusions, such that higher mineralization efficiency is observed with increasing of partial pressure of water. This feature may highlight that during crystallization and cooling, the amounts of released hydrothermal fluids have a decisive role in hydrothermal mineralization, because water-rich magmas generally have higher potential to release hydrothermal fluids (e.g., Richards, 2016).

Based on the results presented here, the compositions of re-equilibrated biotite (formed by re-equilibration of magmatic biotite with exsolved magmatic fluids) could reflect the overall geochemical character of the magmatic-hydrothermal system. For example, a combination of higher Na contents in re-equilibrated biotite and plagioclase (Ab%) are found in the Keder

deposit, while Meiduk is characterized by the lowest Ab% in plagioclase and low contents of Na in the re-equilibrated biotites. In the quartz diorite group, the chloride abundances in biotite decrease from high grade (Dalli, Chahfiruzeh), to Keder low grade deposit, suggesting that chloride content of exsolving fluids in high grade intrusions were probably higher than low grade deposits. Given that high chloride contents have been considered as an important factor in enhancing the ore-forming efficiency of porphyry intrusions, higher chloride contents in the re-equilibrated biotites of Meiduk would be expected compared to the Iju and Sarkuh low grade porphyries that classified as granodiorite. However, chloride contents in biotite at Meiduk are lower than in the studied low grade deposits. As mentioned earlier, Meiduk samples are characterized by the high and scattered log fH$_2$O/fHF and log fH$_2$O/ fHCl values compared to the other deposits (Fig. 11). From this observation and given that chloride is highly incompatible in the biotite structure (because of its larger Cl$^-$ ionic radius compared to OH$^-$), we conclude that that low chloride contents of biotite at Meiduk are most likely related to the modification of biotite halogen chemistry by post-potassic hydrothermal fluids.

Aside from magnetite and hematite crystallization (causal process of sulfate reduction; Sun et al., 2013), during the hydrothermal stage, the thermal history of exsolving hydrothermal fluids seems to be an important factor affecting the stability of metal-transporting chloride complexes and sulfide precipitation. The Cu solubility in such fluids is strongly dependent on temperature, decreasing sharply from ~400 to 300°C (e.g., Landtwing et al., 2005). Cooling of the hydrothermal fluid plays a decisive role in disproportionation of dissolved SO$_2$ to H$_2$S and H$_2$SO$_4$ by the following reaction (Richards, 2011):

$$4SO_2 + 4H_2O \rightleftarrows H_2S + 3H_2SO_4$$
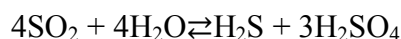
In porphyry copper systems, early sulfide veinlets are mainly emplaced within the zone of potassic alteration (Sillitoe, 2010). However, the bulk of Cu mineralization forms at the end of the potassic alteration process, spatially close to the phyllic alteration (Richards, 2011). Biotite thermometry data indicate that the temperatures of potassic alteration in granodiorite porphyries are lower than those of quartz diorite porphyries. This may be responsible for the copper content in early pyrite associated with potassic alteration. The Cu contents of pyrites in granodiorite porphyries including Meiduk, Iju, and Sarkuh (average 0.137 wt. %) are higher than in the quartz diorite porphyries (Dalli, Chahfiruzeh and Keder; average 0.011 wt. %). Our data indicate that the partitioning of Cu into pyrite associated with early mineralization could be used to discriminate between high grade and low grade deposits because the highest Cu contents were measured in pyrite from high grade porphyries (Dalli, Chahfiruzeh and Meiduk). It should be noted that excess Cu in the pyrites of high grade deposits appear to be related to the presence of micro- to nano-sized inclusions or particles incorporated into the pyrite during growth of the crystals.

The highest temperatures of potassic alteration as documented in the low grade Keder deposit are concomitant with the absence of significant Cu partitioning into pyrite (here Cu content is

14

<0.0001 wt.%), while Meiduk shows the lowest potassic alteration temperature and the highest Cu contents in pyrite. One interpretation of this relationship is that low temperature fluids lead to the high and progressive SO_2 disproportionation to H_2S and H_2SO_4 as observed at the Meiduk deposit. Accordingly, following the sulfide precipitation, high production of H^+ and sulfuric acid could have provided suitable conditions for the development of latter feldspar-destructive alteration at Meiduk compared to other deposits. However, our data show that the more calcic composition (high An% and subsequent Al content) of plagioclase should also be considered as a contributing factor for development of feldspar-disruptive alteration in these porphyry copper systems.

In this study, EMPA analyses and WDS X-ray elemental maps reveal that sulfide mineralization (i.e., pyrite and chalcopyrite) associated with potassic alteration of all selected porphyry deposits contain unexpectedly concentrations of some trace elements. Taken as a whole, the concentrations of trace elements in porphyry deposits in the UDMA appear to be higher than those of other porphyries linked with epithermal systems (e.g., Agua Rica porphyry, Argentina; Franchini et al., 2015; Altar porphyry, Argentina; Maydagan et al., 2013). The lack of significant epithermal systems associated with porphyry systems in UDMA may support the idea that trace elements were retained in the early sulfide mineralization in the porphyry stage and were not leached out and subsequently remobilized during epithermal mineralization stage. However, further work must be carried out to build a better overview on this concept.

5. Conclusion

Combining silicate and sulfide chemistry, we studied the main physicochemical attributes of magmatic – hydrothermal systems associated with high grade and low grade porphyry copper deposits. In order to minimize possible differences related to rock compositions the studied deposits were divided into two major groups: (1) quartz diorite, and (2) granodiorite. The former includes relatively high grade Dalli and Chahfiruzeh porphyries, and a low grade Keder porphyry system, whereas the later includes the large Meiduk deposit, and two low grade deposits at Sarkuh and Iju. Our data indicate that An% and Al content of plagioclase could be linked directly to the magmatic water content of porphyry intrusions. Also, variations in magmatic water coupled with An% and alumina content are strongly associated with the mineralization potential of porphyry intrusions, such that higher mineralization efficiency is observed with increasing of partial pressure of water and increasing An% and Al content of plagioclase. The data indicate that plagioclase composition should also be considered as a key factor in the occurrence and/or expansion of feldspar-destructive alteration (phyllic) in porphyry copper systems, because at acidic pH conditions the dissolution rate would increase with increasing the Al contents of plagioclase. In contrast to low grade deposits (e.g., Keder porphyry), plagioclase in the high grade deposits (e.g., Meiduk porphyry) consistently has high An% and Al content, which could be linked to the expansion of phyllic alteration in the Meiduk deposit compared to those of Keder porphyry. Considering the geochemical characteristics of reequilibrated biotite associated with early sulfide mineralization at low grade and high grade porphyry copper

systems, it is shown that a combination of higher chloride and low temperatures are involved during the early sulfide mineralization at high grade porphyry copper systems. Nevertheless, the incompatibility of chloride in biotite structure and subsequent modification of biotite halogen chemistry by post-potassic hydrothermal fluids may produce low chloride contents in some high grade deposits (i.e., Meiduk porphyry). Our sulfide data indicate that the copper contents of pyrites associated with early stages of mineralization might be used to discriminate between between high grade and low grade deposits because the highest Cu contents (occurring mostly as micro- to nano-sized inclusions/particles) were observed in pyrites from high grade porphyries. Sulfides in early mineralization stage of all selected PCDs also contain unexpectedly high concentrations of Te, Se, and Re that may be important for extraction as by-products of Cu production.

Acknowledgements

References

Afshooni, S.Z., Mirnejad, H., Esmaeily, D. and Haroni, H.A. (2013) Mineral chemistry of hydrothermal biotite from the Kahang porphyry copper deposit (NE Isfahan), Central Province of Iran. *Ore Geology Reviews* **54**, 214–232.

Agard, P., Omrani, J., Jolivet, L. and Mouthereau, F. (2005) Convergence history across Zagros, Iran: constraints from collisional and earlier deformation. *International Journal of Earth Sciences* **94**, 401–419.

Aghazadeh, M., Hou, Z., Badrzadeh, Z. and Zhou, L. (2015) Temporal–spatial distribution and tectonic setting of porphyry copper deposits in Iran: Constraints from zircon U–Pb and molybdenite Re–Os geochronology. *Ore Geology Reviews* **70**, 385-406.

Alavi, M. (2007) Structures of the Zagros fold-thrust belt in Iran. *American Journal of Science* **307**, 1064–1095.

Asadi, S. (2013) Geochemistry of selected productive and barren intrusions in Shahr Babak copper complex, Urumiyeh–Dokhtar volcano-magmatic belt. Ph. D. thesis, Shiraz University.

Asadi, S., Mathur, R., Moore, F. and Zarasvandi, A. (2015) Copper isotope fractionation in the Meiduk porphyry copper deposit, northwest of Kerman Cenozoic magmatic arc, Iran. *Terra Nova* **27**, 36-41.

Asadi, S., Moore, F. and Zarasvandi, A. (2014) Discriminating productive and barren porphyry copper deposits in the southeastern part of the central Iranian volcano-plutonic belt, Kerman region, Iran: a review. *Earth-Science Reviews* **138**, 25-46.

Audetat, A., Pettke, T., Heinrich, C.A. and Bodnar, R. (2008) The composition of magmatic–hydrothermal fluids in barren and mineralized intrusions. *Economic Geology* **103**, 877–908.

Ayati, F., Yavuz, F., Haroni, H.A., Richards, J.P. and Jourdan, F. (2013) Petrology and geochemistry of calc-alkaline volcanic and subvolcanic rocks, Dalli porphyry copper–gold deposit, Markazi Province, Iran. *International Geology Review* **55**, 158–184.

Ayati, F., Yavuz, F., Noghreyan, M., Haroni, A. and Yavuz, R. (2008) Chemical characteristics and composition of hydrothermal biotite from the Dalli porphyry copper prospect, Arak, central province of Iran. *Mineralogy and Petrology* **94**, 107–122.

Ayres, R.U., Ayres, L. and Råde, I. (2002) The Life Cycle of Copper, Its Co-products and Byproducts (http://pubs.iied.org/pdfs/G00740.pdf).

Barzegar, H. (2007) Geology, petrology and geochemical characteristics of alteration zones within the Seridune prospect, Kerman, Iran. Ph.D. thesis, Aachen University.

Beane, R.E. (1978) Biotite stability in the porphyry copper environment. *Economic Geology* **69**, 241–256.

Bonatti, E. (1987) Oceanic evolution, rifting or drifting in the Red Sea. *Nature* **330**, 692–693.

Boomeri, M., Nakashima, K. and Lentz, D.R. (2009) The Miduk porphyry Cu deposit, Kerman, Iran: a geochemical analysis of the potassic zone including halogen element systematics related to Cu mineralization processes. *Journal of Geochemical Exploration*, **103**, 17–29.

Boomeri, M., Nakashima, K. and Lentz, D.R. (2010) The Sar-Cheshmeh porphyry copper deposit, Kerman, Iran: a mineralogical analysis of the igneous rocks and alteration zones including halogen element systematics related to Cu mineralization processes. *Ore Geology Reviews*, **38**, 367–381.

Chen, J.L., Xu, J.F., Wang, B.D., Yang, Z.M., Ren, J.B., Yu, H.X., Liu, H. and Feng, Y. (2015) Geochemical differences between subduction- and collision-related copper-bearing porphyries and implications for metallogenesis. *Ore Geology Reviews* **70**, 424-437.

Cioacă, M.E., Munteanu, M., Qi, L. and Costin, C. (2014) Trace element concentrations in porphyry copper deposits from Metaliferi Mountains, Romania: A reconnaissance study. *Ore Geology Reviews* **63**, 22–39.
.

Cook, N.J. and Ciobanu, C.L. (2004) Bismuth tellurides and sulphosalts from the Larga hydrothermal system, Metaliferi Mts., Romania: paragenesis and genetic significance. *Mineralogical Magazine* **68**, 301–321.

Cook, N.J., Ciobanu, C.L., Danyushevsky, L.V. and Gilbert, S. (2011) Minor and trace elements in bornite and associated Cu–(Fe)–sulfides: LA-ICP-MS study. *Geochimica et Cosmochimica Acta* **75**, 6473–6496.

Cox, D.P. and Singer, D.A. (1988) Distribution of gold in porphyry copper deposits. *US Geological Survey,* Open-file Report.

Davidson, J., Turner, S., Handley, H., Macpherson, C. and Dosseto, A. (2007) Amphibole ''sponge'' in arc crust?. *Geology* **35**, 787–790.

Dehghani, G.A. and Makris, T. (1983) The gravity field and crustal structure of Iran. *Geological Survey of Iran*, Report **51**, 51–68.

Dercourt, J., Zonenshain, L., Ricou, L.E., Kazmin, G., Le Pichon, X., Knipper, A.L., Grandjacquet, C., Sbortshikov, I.M., Geyssant, J., Lepvrier, C., Pechersky, D.H., Boulin, J., Sibuet, J.C., Savostin, L.A., Sorokhtin, O., Westphal, M., Bazhenov, M.L., Lauer, J.P. and Bijou-Duval, B. (1986) Geological evolution of the Tethys belt from the Atlantic to Pamirs since the Lias. *Tectonophysics* **123**, 241–315.

Einali, M., Alirezaei, S. and Zaccarini, F. (2014) Chemistry of magmatic and alteration minerals in the Chahfiruzeh porphyry copper deposit, south Iran: implications for the evolution of the magmas and physicochemical conditions of the ore fluids. *Turkish Journal of Earth Sciences* **23**, 147-165.

Franchini, M., McFarlane, C., Maydagán, L., Reich, M., Lentz, D.R, Meinert, L. and Bouhier, V. (2015) Trace metals in pyrite and marcasite from the Agua Rica porphyry-high sulfidation epithermal deposit, Catamarca, Argentina: Textural features and metal zoning at the porphyry to epithermal transition. *Ore Geology Reviews*, **66**, 366–387.

Ghorbani, M. and Ebrahimi, M. (2009) Tertiary-Quaternary magmatism in the Dehaj area. *Earth and Recourse Journal* **1**, 77-89.

Grew, E.S., Yates, M.G., Shearer, C.K., Hagerty, J.J., Sheraton, J.W. and Sandiford, M. (2006) Beryllium and other trace elements in paragneisses and anatectic veins of the ultrahigh-temperature Napier Complex, Enderby Land, East Antarctica: the role of sapphirine. *Journal of Petrology* **47**, 859–882.

Guiraud, R. and Bosworth, W. (1997) Senonian basin inversion and rejuvenation of rifting in Africa and Arabia: synthesis and implications to plate-scale tectonics. *Tectonophysics* 282, 39–82.

Harouiya, N. and Oelkers, E.H. (2004) An experimental study of the effect of aqueous fluoride on quartz and alkali-feldspar dissolution rates. *Chemical Geology* **205**, 155–167.

Haschke, M., Ahmadian, J., Murata, M. and McDonald, I. (2010) Copper mineralization prevented by arc-root delamination during Alpine–Himalayan collision in Central Iran. *Economic Geology* **105**, 855–865.

Hassanzadeh, J. (1993) Metallogenic and tectono-magmatic events in the SE sector of the Cenozoic active continental margin of Iran (Shahr-e-Babak area, Kerman province). Ph.D. thesis, University of California.

Harris, A.C. and Golding, S.D., (2002) New evidence of magmatic-fluid–related phyllic alteration: Implications for the genesis of porphyry Cu deposits. *Geology* **30**, 335-338.

Hattori, K. and Sato, H. (1996) Magma evolution recorded in plagioclase zoning in 1991 Pinatubo eruption products. *American Mineralogist* **81**, 982–994.

Hedenquist, J.W. and Lowenstern, J.B., (1994) The role of magmas in the formation of hydrothermal ore deposits. *Nature* **370**, 519–527.

Henry, D.J., Guidotti, C.V. and Thomson, J.A. (2005) The Ti-saturation surface for lowtomedium pressure metapelitic biotite: implications for geothermometry and Ti-substitution mechanisms. *American Mineralogist* **90**, 316–328.

Hezarkhani, A. and Williams-Jones, A.E. (1998) Controls of alteration and mineralization in the Sungun Porphyry Copper Deposit, Iran: evidence from fluid inclusions and stable isotopes. *Economic Geology* **93**, 651–670.

Hou, Z.Q., Yang, Z.M., Qu, X.M.,Meng, X.J., Li, Z.Q., Beaudoin, G., Rui, Z.Y., Gao, Y.F. and Khin, Z. (2009) The Miocene Gangdese porphyry copper belt generated during post-collisional extension in the Tibetan orogen. *Ore Geology Reviews* **36**, 25–51.

Jacobs, D.C. and Parry, W.T. (1979) Geochemistry of biotite in the Santa Rita porphyry copper deposit, New Mexico. *Economic Geology* **74**, 860–887.

Kazemi-Mehrnia, A. (2010) Characteristics of leached capping and evolution of supergene enrichment of Northwest Kerman belt copper-molybdenum porphyry deposits. Ph.D. thesis, University of Shahid Beheshti.

Kyono, A. and Kimata, M. (2001) Refinement of the crystal structure of a synthetic non-stoichiometric Rb-feldspar. *Mineralogical Magazine* **65**, 523–531.

Landtwing, M.R., Pettke, T., Halter, W.E., Heinrich, C.A., Redmond, P.B., Einaudi, M.T. and Kunze, K. (2005) Copper deposition during quartz dissolution by cooling magmatic–hydrothermal fluids: the Bingham porphyry. *Earth and Planetary Science Letters* **235**, 229–243.

Liang, H.Y., Campbell, I.H., Allen, C., Sun, W.D., Liu, C.Q., Yu, H.X., Xie, Y.W. and Zhang, Y.Q. (2006) Zircon Ce^{4+}/Ce^{3+} ratios and ages for Yulong ore-bearing porphyries in eastern Tibet. *Mineralium Deposita* **41**, 152–159.

Maydagan, L., Franchini, M., Impiccini, A. and Lentz, D.R. (2016) Phyllosilicates geochemistry and distribution in the Altar porphyry Cu- (Au) deposit, Andes Cordillera of San Juan, Argentina: Applications in exploration, geothermometry, and geometallurgy. *Journal of Geochemical Exploration* **167**, 83-109.

Maydagán, L., Franchini, M.B., Lentz, D., Pons, J. and McFarlane, C. (2013) Sulfide composition and isotopic signature of the Altar Cu–Au deposit, Argentina: constraints on the evolution of the porphyry–epithermal system. *Canadian Mineralogist* **51**, 813–840.

McClay, K.R., Whitehouse, P.S., Dooley, T. and Richards, M. (2004) 3D evolution of fold and thrust belts formed by oblique convergence. *Marine Geology* **21**, 857–877.

McClusky, S., Reilinger, R., Mahmoud, S., Ben Sari, D. and Tealeb, A. (2003) GPS constraints on Africa (Nubia) and Arabia plate motion. *Geophysical Journal International* **155**, 126–138.

McInnes, B.I.A., Evans, N.J., Belousova, E., Griffin, W.T. and Andrew, R.L. (2003) Timing of mineralization and exhumation processes at the Sar Cheshmeh and Meiduk porphyry Cu deposits, Kerman belt, Iran. In Mineral exploration and sustainable development (eds. Eliopoulos et al.). Rotterdam, Mill Press. pp. 1197–1200.

McInnes, B.I.A., Evans, N.J., Fu, F.Q., Garwin, S., Belousova, E., Griffin, W.L., Bertens, A., Sukama, D., Permanadewi, S., Andrew, R.L. and Deckart, K. (2005) Thermal history analysis of selected Chilean, Indonesian, and Iranian porphyry Cu–Mo–Au deposits. In Super Porphyry Copper and Gold Deposits: A Global Perspective (e.d. T.M. Porter)., PGC publishing, Adelaide. pp. 1–16.

Mercer, C. and Reed, M. (2013) Porphyry Cu-Mo stockwork formation by dynamic, transient hydrothermal pulses: mineralogic insights from the deposit at Butte, Montana. *Economic Geology* **108**, 1347–1377.

Mirnejad, H., Mathur, R., Hassanzadeh, J., Shafie, B. and Nourali, S. (2013) Linking Cu mineralization to host porphyry emplacement: Re-Os ages of molybdenites versus U-Pb ages of zircons and sulfur isotope compositions of pyrite and chalcopyrite from the Iju and Sarkuh porphyry deposits in Southeast Iran. *Economic Geology* **108**, 861-870.

Mohajjel, M., Fergusson, C.L. and Sahandi, M.R. (2003) Cretaceous–Tertiary convergence and continental collision, Sanandaj–Sirjan zone, western Iran. *Journal of Asian Earth Sciences* **21**, 397–412.

Mohammadzadeh, Z. (2009) Geology, alteration and copper mineralization in Chahfiruzeh area, Share-Babak, Kerman province. M.Sc thesis, University of Shahid Beheshti.

Munoz, J.L. (1992) Calculation of HF and HCl fugacities from biotite compositions: revised equations. *Geological Society of America*, Abstract with Programs 24, p. 221.

Munoz, J.L. and Ludington, S.D. (1974) Fluoride-hydroxyl exchange in biotite. *American Journal of Science* **274**, 396−413.

Nachit, H., Ibhi, A.B., Abia, El-H., El Hassan, A. and Ben Ohoud, M. (2005) Discrimination between primary magmatic biotites, reequilibrated biotites, and neoformed biotites. *Comptes Rendus Geoscience* **337**, 1415–1420.

Nachit, H., Razafimahefa, N., Stussi, J.M. and Carron, J.P. (1985) Composition chimique des biotites et typologie magmatique des granitoides. *Comptes rendus hebdomadaires des séances* **301**, 813–818.

Nourali, S. (2011) Mineralization modeling and genesis of Sarkuh porphyry copper deposit, Kerman. M.Sc thesis, University of Tehran.

Nourali, S. and Mirnejad, H. (2012) Hydrothermal evolution of the Sarkuh porphyry copper deposit, Kerman, Iran: A fluid inclusion and sulfur isotope investigation. *Geopersia* **2**, 93-107.

Palenik, C.S., Utsunomiya, S., Reich, M., Kesler, S.E. and Ewing, R.C. (2004) "Invisible" gold revealed: direct imaging of gold nanoparticles in a Carlin-type deposit. *American Mineralogist* **89**, 1359–1366.

Parsapoor, A., Khalili, M., Tepley, F. and Maghami, F. (2015) Mineral chemistry and isotopic composition of magmatic, re-equilibrated and hydrothermal biotites from Darreh-Zar porphyry copper deposit, Kerman (Southeast of Iran). *Ore Geology Reviews* **66**, 200–218.

Pirajno, F. (2009) *Hydrothermal processes and mineral systems*. Geological Survey of Western Australia, Springer.

Popescu, Gh., Neacşu, A., Cioacă, M. and Buia, G. (2013) Tellurium, selenium and cadmium resources in the waste dumps of Săcărâmb area (Apuseni Mountains), Romania. *Carpathian Journal of Earth and Environmental Science* **8**, 199–206.

Reich, M., Deditius, A., Chryssoulis, S., Li, J.W., Ma, C.Q., Parada, M.A., Barra, F. and Mittermayr, F. (2013a) Pyrite as a record of hydrothermal fluid evolution in porphyry copper system: a SIMS/EMPA trace element study. *Geochimica et Cosmochimica Acta* **104**, 42–62.

Reich, M., Kesler, S.E., Utsunomiya, S., Palenik, C., Chryssoulis, S.L. and Ewing, R.C. (2005) Solubility of gold in arsenian pyrite. *Geochimica et Cosmochimica Acta* 69, 2781‑2796.

Reich, M., Palacios, C., Barra, F. and Chryssoulis, S. (2013b) "Invisible" silver in chalcopyrite and bornite from the Mantos Blancos Cu deposit, northern Chile. *European Journal of Mineralogy* **25**, 453–460.

Rezaei, M. (2017) Effective parameters in mineralization potential of economic and sub-economic porphyry copper deposits in Urumieh-Dokhtar magmatic zone: using geochemical and fluid inclusion studies. Ph.D. thesis, Shahid Chamran University, Ahvaz.

Richards, J.P. (2003) Tectono-magmatic precursors for porphyry Cu–(Mo–Au) deposit formation. *Economic Geology* **98**, 1515–1533.

Richards, J.P. (2011) Magmatic to hydrothermal metal fluxes in convergent and collided margins. *Ore Geology Reviews* **40**, 1–26.

Richards, J.P. (2013) Giant ore deposits formed by optimal alignments and combinations of geological processes. *Nature Geoscience* **6**, 911-916.

Richards, J.P. (2015a) Introduction to special issue: Magmatic and metallogenic evolution of the Tethyan Orogen. *Ore Geology Reviews* **70**, 321–322.

Richards, J.P. (2015b) Tectonic, magmatic, and metallogenic evolution of the Tethyan orogen: From subduction to collision. *Ore Geology Reviews* **70**, 323-345.

Richards, J.P. (2016) Clues to hidden copper deposits. *Nature Geoscience* **9**, 1-2.

Richards, J.P., Spell, T., Rameh, E., Razique, A. and Fletcher, T. (2012) High Sr/Y magmas reflect arc maturity, high magmatic water content, and porphyry Cu $\pm$ Mo $\pm$ Au potential: examples from the Tethyan arcs of Central and Eastern Iran and Western Pakistan. *Economic Geology* **107**, 295–332.

Robert, J.L. (1976) Titanium solubility in synthetic phlogopite solid solutions. *Chemical Geology* **17**, 213–227.

Roşu, E., Szakacs, A., Downes, H., Seghedi, I. and Peckskay, Z. (2004) Timing of Miocene–Quaternary magmatism and metallogeny in the South Apuseni Mountains, Romania. *Romanian Journal of Mineral Deposits* **81**, 33–38.

Selby, D. and Nesbitt, B.E. (2000) Chemical composition of biotite from Casino porphyry Cu–Au–Mo mineralization, Yukon, Canada: evaluation of magmatic and hydrothermal fluid chemistry. *Chemical Geology* **171**, 77–93.

Shafiei, B. and Shahabpour, J. (2008) Gold distribution in porphyry copper deposits of Kerman region, southeastern Iran. *Journal of Sciences, Islamic Republic of Iran* **19**, 247–260.

Shafiei, B., Haschke, M. and Shahabpour, J. (2009) Recycling of orogenic arc crust triggers porphyry Cu mineralization in Kerman Cenozoic arc rocks, southeastern Iran. *Mineralium Deposita* **44**, 265–283.

Shahabpour, J. (2005) Tectonic evolution of the orogenic belt in the region located between Kerman and Neyriz. *Journal of Asian Earth Sciences* **24**, 405–417.

Shannon, R.D. (1976) Revised effective ionic radii and systematic studies of interatomic distances in halides and chalcogenides. *Acta Crystallographica* **32**, 751–767.

Sillitoe, R.H. (2010) Porphyry copper systems. *Economic Geology* **105**, 3–41.

Stillings, L.L., Drever, J.I., Brantley, S.L., Sun, Y.T. and Oxbergh, R. (1996) Rates of feldspar dissolution at pH 3–7 with 0–8 mM oxalic acid. *Chemical Geology* **132**, 79‑89.

Sun,W.D., Liang, H.Y., Ling, M.X., Zhan, M.Z., Ding, X., Zhang, H., Yang, X.Y., Li, Y.L., Ireland, T.R.,Wei, Q.R. and Fan,W.M. (2013) The link between reduced porphyry copper deposits and oxidized magmas. *Geochim. Cosmochim. Acta* **103**, 263–275.

Taghinejad, A. (2012) Petrology, alteration and copper mineralization in Keder area, Shahr-e-babak, Kerman province. M.Sc thesis, Islamic Azad University.

Taghipour, N., Aftabi, A. and Mathur, R. (2008) Geology and Re-Os Geochronology of Mineralization of the Miduk Porphyry Copper Deposit, Iran. *Resource Geology* **58**, 143-160.

Teiber, H., Scharrer, M., Marks, M.A.W., Arzamastsev, A.A., Wenzel, T. and Markl, G. (2015) Equilibrium partitioning and subsequent re-distribution of halogens among apatite–biotite–amphibole assemblages from mantle-derived plutonic rocks: Complexities revealed. *Lithos* **220**, 221–237.

Tischendorf, G., Gottesmann, B., Förster, H.J. and Trumbull, R.B. (1997) On Li-bearing micas: estimating Li from electron microprobe analyses and an improved diagram for graphical representation. *Mineralogical Magazine* **61**, 809–834.

Ushioda, M., Takahashi, E., Hamada, M. and Suzuki, T. (2014) Water content in arc basaltic magma in the Northeast Japan and Izu arcs: an estimate from Ca/Na partitioning between plagioclase and melt. *Earth, Planets and Space* **66**, 127-137.

Wang, R., Richards, J.P., Hou, Z., Yang, Z. and Dufrane, A. (2014a) Increased magmatic water content—the key to Oligo–Miocene porphyry Cu–Mo $\pm$ Au formation in the Eastern Gangdese Belt, Tibet. *Economic Geology* **109**, 1315–1339.

Wang, R., Richards, J.P., Hou, Z.Q., Yang, Z.M., Gou, Z.B. and DuFrane, A. (2014b) Increasing magmatic oxidation state from Paleocene to Miocene in the eastern Gangdese belt, Tibet: Implication for collision-related porphyry Cu-Mo $\pm$ Au mineralization. *Economic Geology* **109**, 1943‑1965.

Williamson, B. J., Herrington, R. J. and Morris, A. (2016) Porphyry copper enrichment linked to excess aluminium in plagioclase. *Nature Geoscience* **9**, 237-241.

Zarasvandi, A., Liaghat, S. and Zentilli, K. (2005) Porphyry copper deposits of the Urumieh–Dokhtar magmatic arc, Iran. In Super porphyry copper and gold deposits: A Global Perspective (e.d. T.M. Porter). Porter Geoscience Consulting Press, Australia. pp. 441–452.

Zarasvandi, A., Liaghat, S., Lentz, D. and Hossaini, M. (2013) Characteristics of mineralizing fluids of the Darreh-Zerreshk and Ali-Abad porphyry copper deposits, Central Iran, determined by fluid inclusion microthermometry. *Resource Geology* **63**, 188–209.

Zarasvandi, A., Rezaei, M., Sadeghi, M., Lentz, D.R, Adelpour, M. and Pourkaseb, H. (2015a) Rare earth element signatures of economic and sub-economic porphyry copper systems in Urumieh–Dokhtar magmatic arc (UDMA), Iran. *Ore Geology Reviews* **70**, 407-423.

Zarasvandi, A., Rezaei, M., Raith, J.G., Lentz, D.R., Azimzadeh, A.M. and Pourkaseb, H. (2015b) Geochemistry and fluid characteristics of the Dalli porphyry Cu–Au deposit, Central Iran. *Journal of Asian Earth Sciences* **111**, 175–191.

Zhang, L. and Luttge, A. (2009) Theoretical approach to evaluating plagioclase dissolution mechanisms. *Geochimica et Cosmochimica Acta* **73**, 2832–2849.

Zhang, W., Lentz, D.R., Thorne, K.G. and McFarlane, C. (2016) Geochemical characteristics of biotite from felsic intrusive rocks around the Sisson Brook W–Mo–Cu deposit, west-central New Brunswick: An indicator of halogen and oxygen fugacity of magmatic systems. *Ore Geology Reviews* **77**, 82–96.

Zhu, C. and Sverjensky, D.A. (1991) Partitioning of F–Cl–OH between minerals and hydrothermal fluids. *Geochimica et Cosmochimica Acta* **55**, 1837–1858.

Zhu, C. and Sverjensky, D.A. (1992) F–Cl–OH partitioning between biotite and apatite. *Geochimica et Cosmochimica Acta* **56**, 3435–3467.

Figure captions

Fig. 1. Location of selected high grade and low grade porphyry copper deposits (except for Dalli deposit) in the northwestern part of Kerman Cenozoic magmatic arc (KCMA), which is the southeastern segment of Urumieh-Dokhtar magmatic arc. Modified after Shafiei et al. (2009).

Fig. 2. SiO_2 vs. $CaO + Na_2O + K_2O$ (wt. %) diagram. Muscovite, illite, mullite, kaolinite and K-feldspar array after Williamson et al. (2016).

Fig. 3. (A) Classification of biotite on the (Mg-Li) vs. ($Fe_{tot}+Mn+Ti–Al^{VI}$) diagram (Tischendorf et al., 1997), (B) $10*(TiO_2)$ - $FeO_{tot} + MnO$ - MgO ternary diagram of biotite from high grade and low grade porphyry copper systems. Fields of primary, re-equilibrated and secondary bioite according to Nachit et al. (1985, 2005).

Fig. 4. Histograms showing Na and Ti (apfu) and Fe/(Fe + Mg) of re-equilibrated biotite from the potassic alteration zone of high grade and low grade PCDs. See text for explanations.

23

Fig. 5. (A) Molar fractions of F (X_F), and (B) Cl (X_{Cl}) of re-equilibrated biotite from the potassic alteration zone of studied PCDs.

Fig. 6. Al/(Ca + Na + K) (*apfu*) vs. An%. Fields of barren calc-alkaline rocks and calc-alkaline rocks with associated PCD after Williamson et al. (2016).

Fig. 7. Diagram of Al + Si (*a.p.f.u.*) vs. Ca + Na + K (*a.p.f.u.*), showing negative correlation between these parameters. Black arrows show the exchange vectors based on MT_4O_8 ideal formula of feldspar (Williamson et al., 2016).

Fig. 8. Diagram showing anorthite content of plagioclase (An %) for high grade to low grade porphyries. (A) granodiorite group, (B) quartz diorite group.

Fig. 9. Results of biotite geothermometry (Beanne, 1978). Biotite is from the potassic alteration zone. (A) quartz diorite group, and (B) granodiorite group.

Fig. 10. X_{Mg} vs. log (X_F/X_{Cl}) diagrams for quartz-diorite (A), and granodiorite porphyries (B). X_{Mg} vs. log (X_F/X_{OH}) diagrams for quartz-diorite (C), and granodiorite porphyries (D). Fields of Sarcheshmeh porphyry deposit after Boomeri et al. (2010). See text for explanation.

Fig. 11. Comparison of fugacity ratios of this study with other porphyry Cu systems. Field of Sarcheshmeh after Boomeri et al., 2010), and Bingham after Selby and Nesbitt (2000).

Fig. 12. Concentration of Au vs. As (ppm) in pyrite. The dashed line divides the fields of Au substitution in the pyrite structure as Au^+ from Au^0 present in inclusions (Reich et al., 2005). Field of Dexing porphyry deposit after Reich et al. (2013a). Field of Colnic and Rovina porphyry deposits from Cioacă et al. (2014).

Fig. 13. Binary plot of Au vs. As for pyrite analysis from the high grade and low grade deposits.

Fig. 14. Back-scattered electron (BSE) image (A), and wavelength-dispersive spectrometry (WDS) X-ray elemental maps showing the distribution of Cu, Fe, Ni, Mo and Au in the early pyrite and chalcopyrite associated with potassic alteration of Meiduk porphyry copper deposit (B-F; respectively).

Fig. 15. Back-scattered electron (BSE) image (A), and wavelength-dispersive spectrometry (WDS) X-ray elemental maps showing Cu, S, Co, Ni and Mo in early pyrite and chalcopyrite associated with potassic alteration of Keder low grade deposit (B-F; respectively). Chalcopyrite occurs as fracture filling in pyrite.
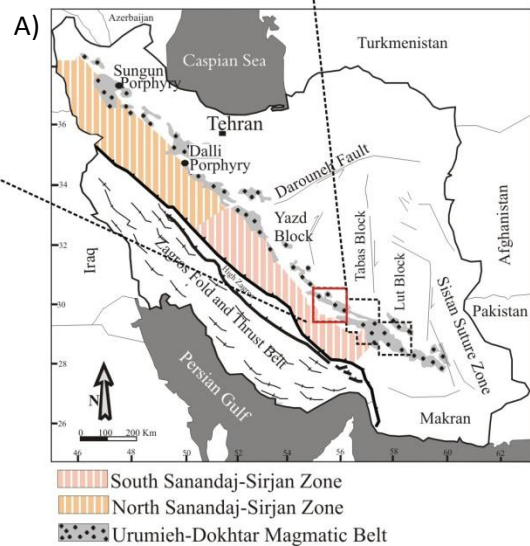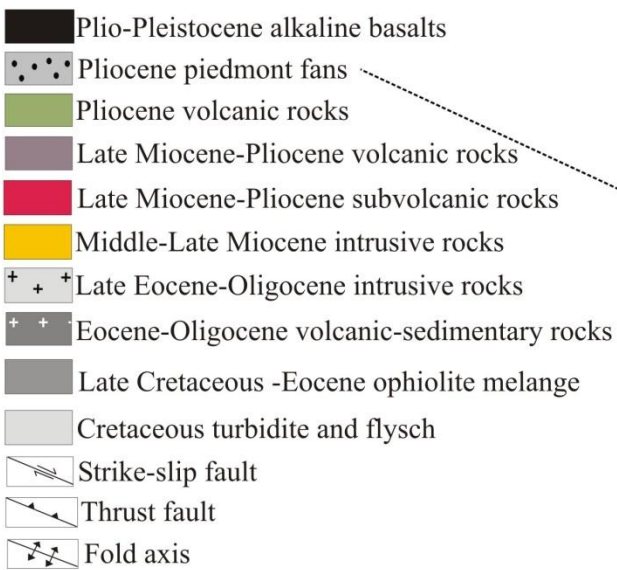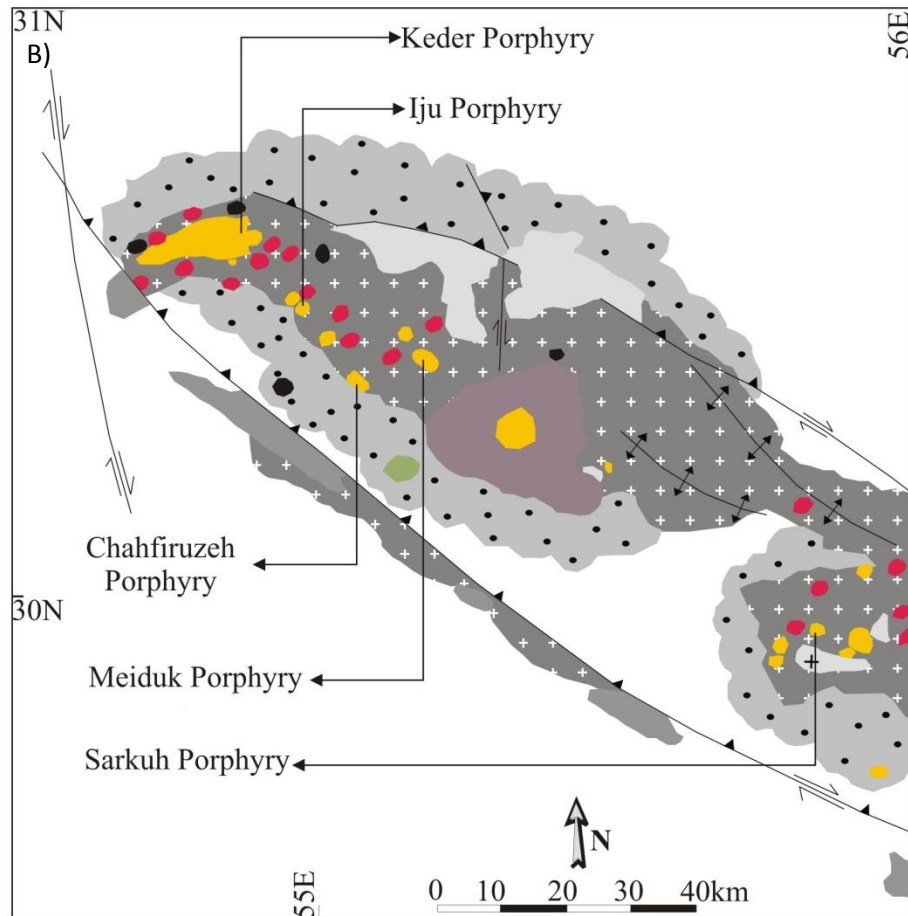
Fig. 1.
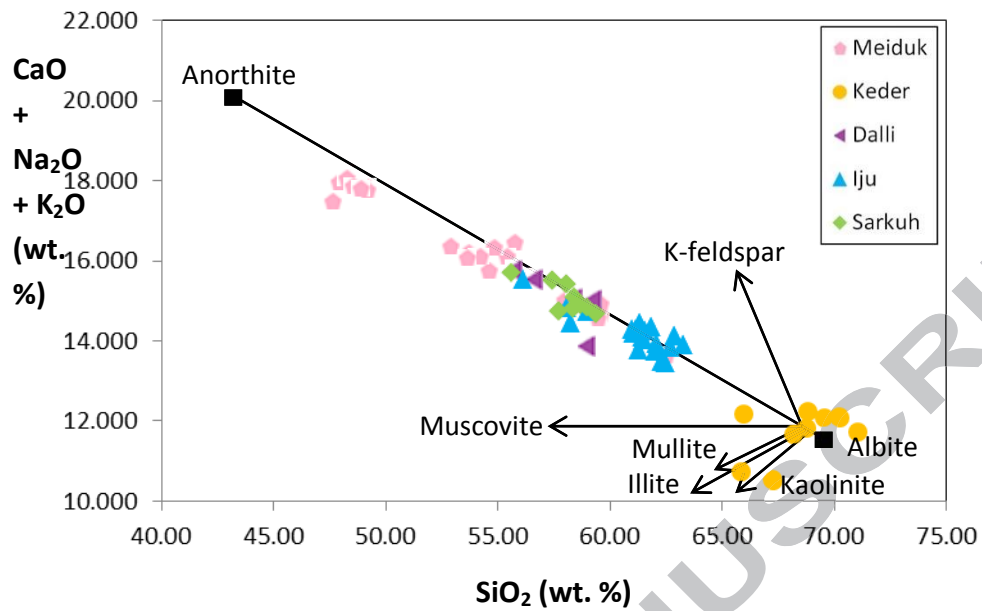
Fig. 2.
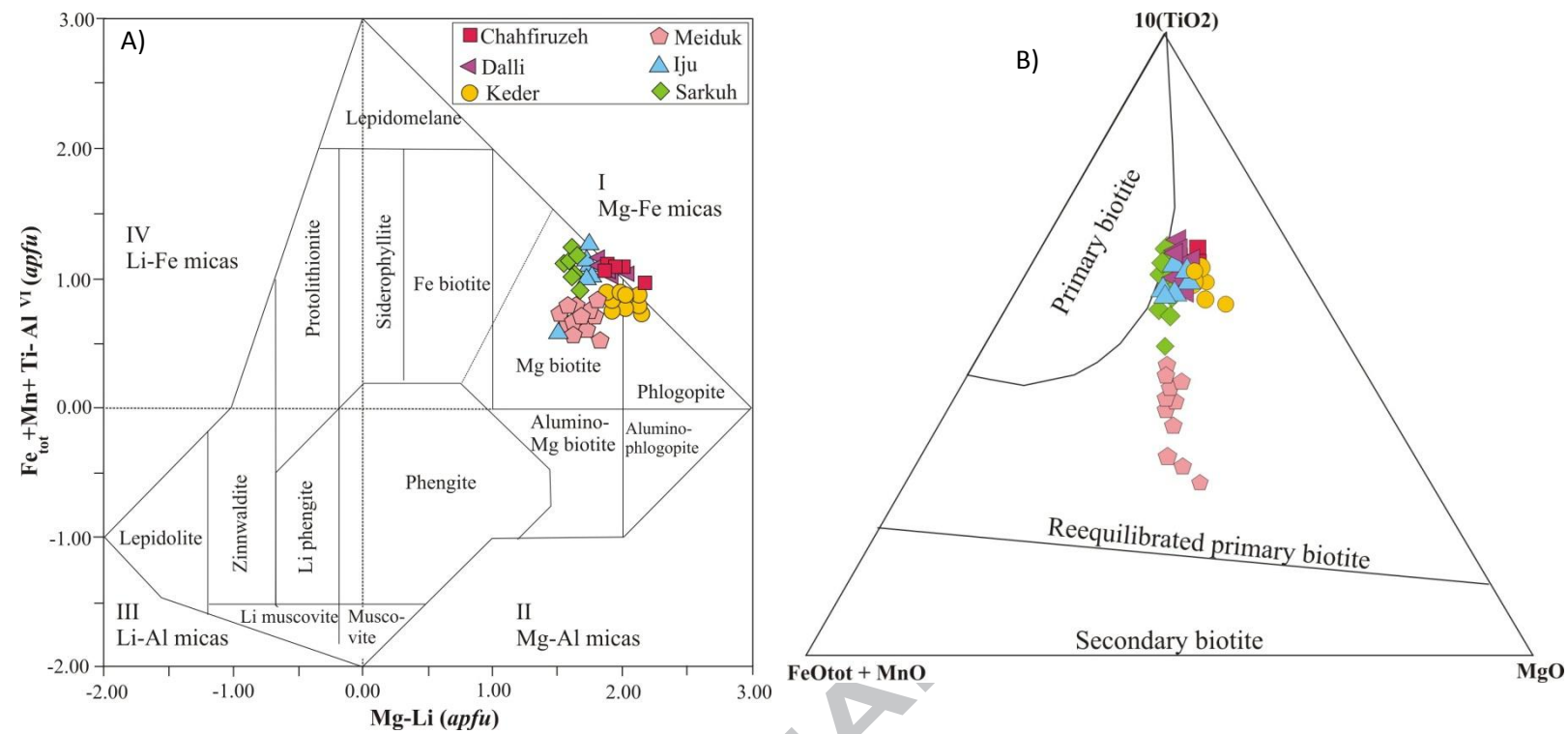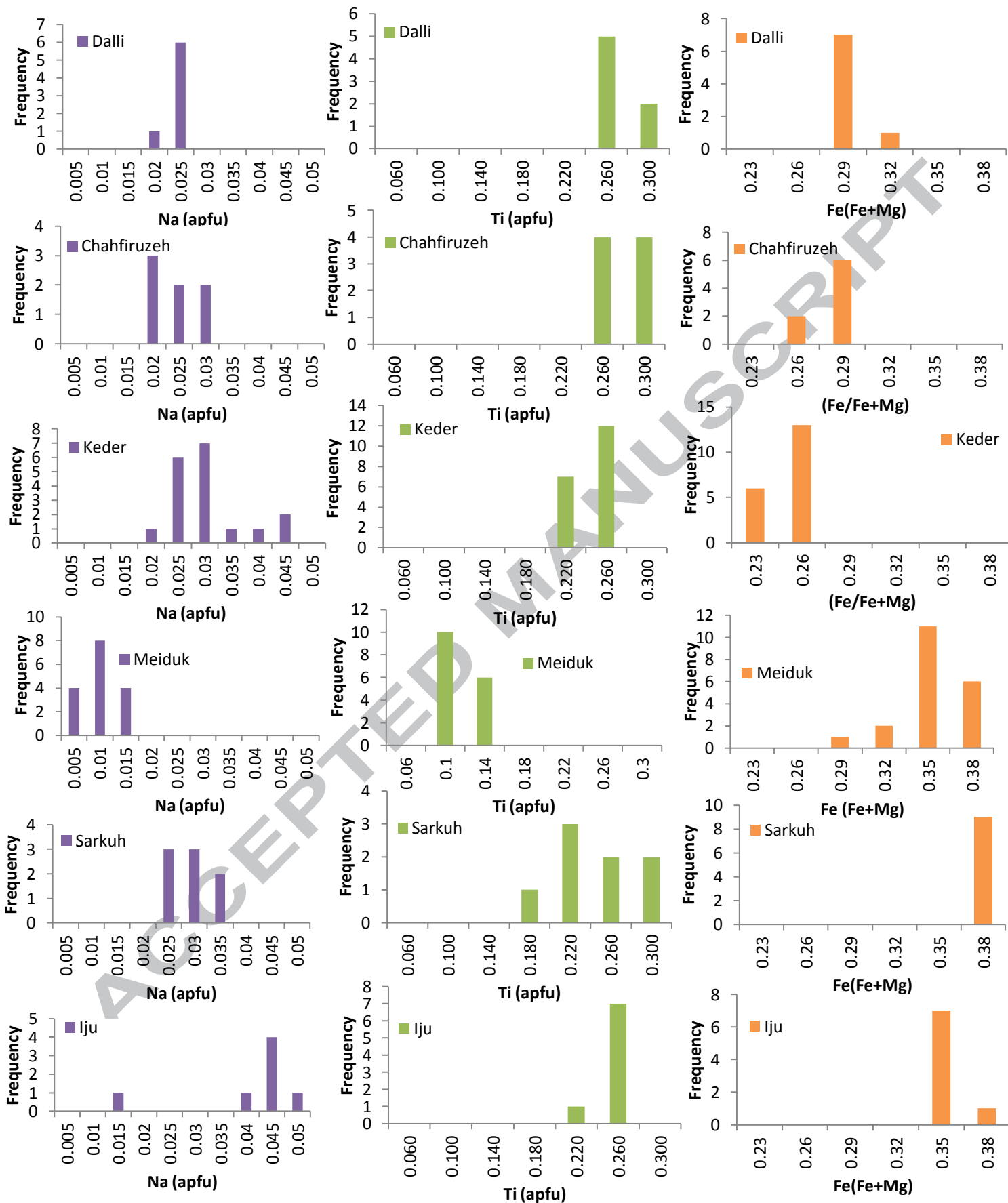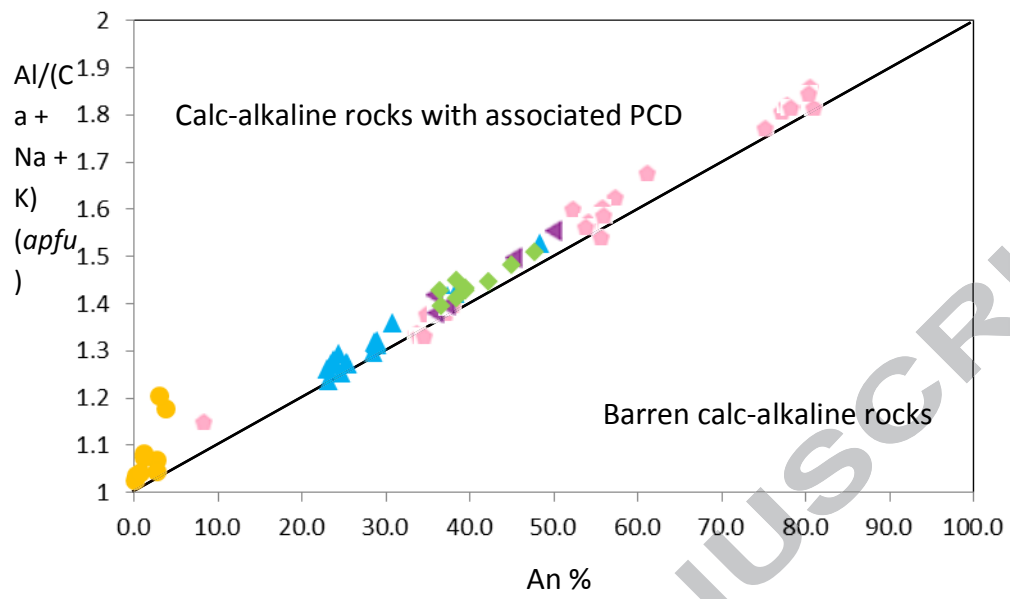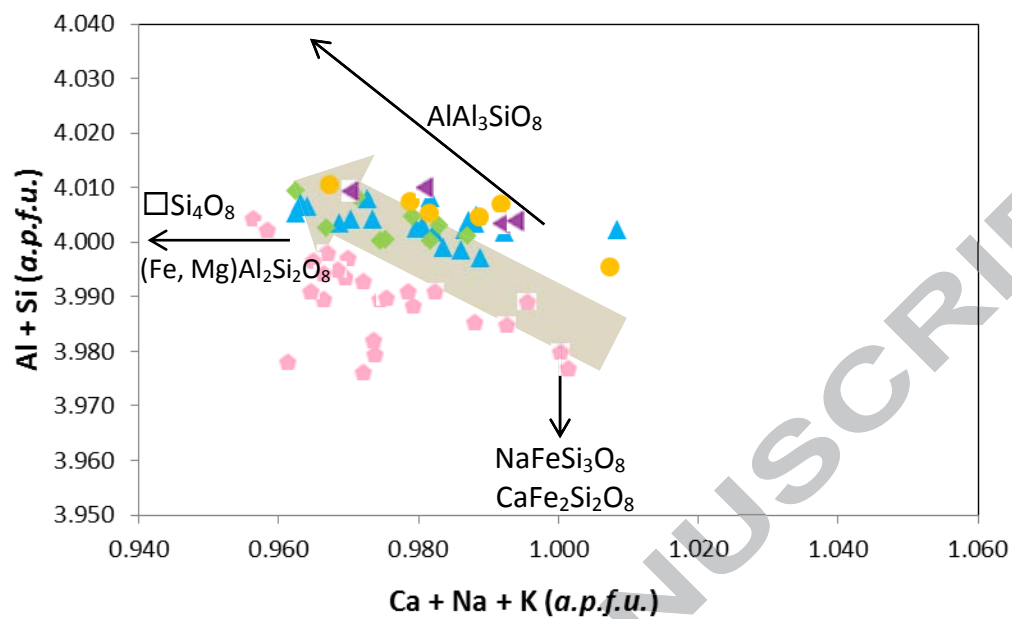
Fig. 3.

27

Fig. 4

28

Fig. 6.

Fig. 7.

Fig. 8.
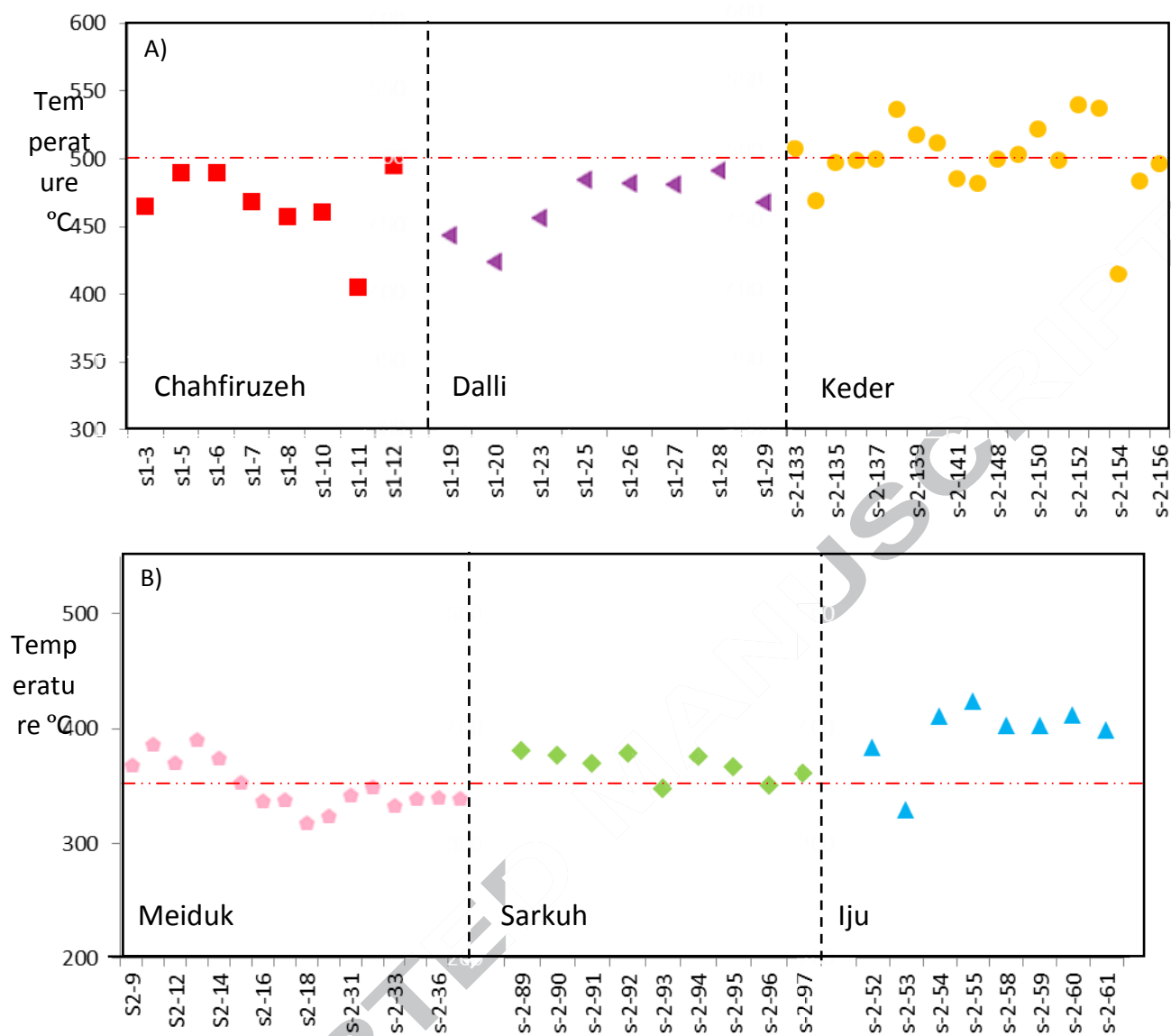
Fig. 9.
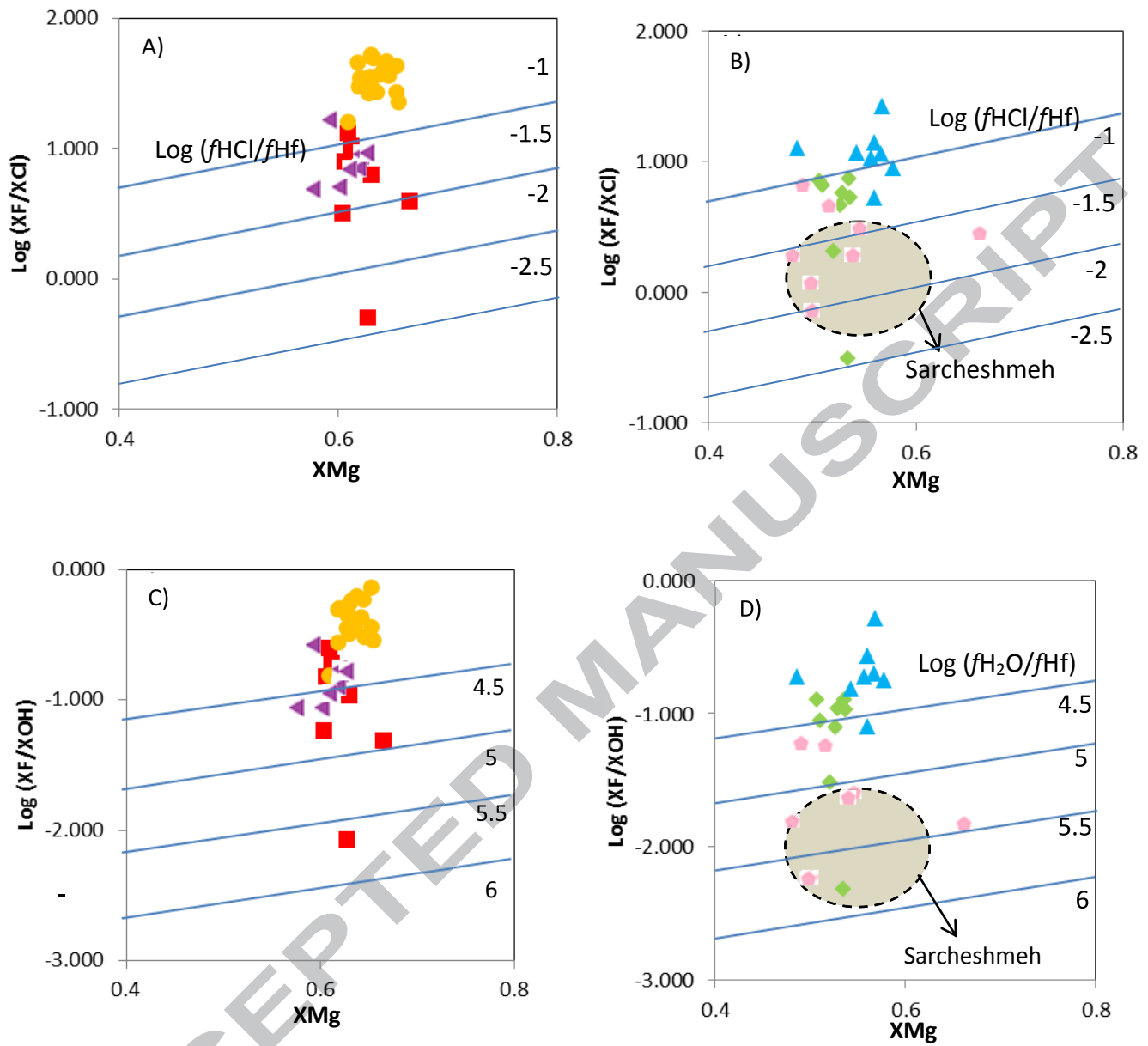
Fig. 10.
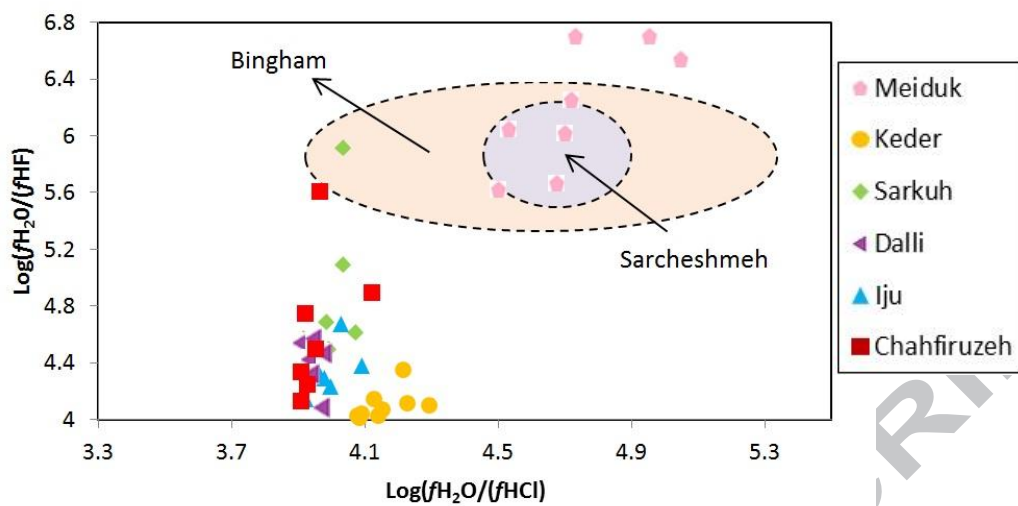
Fig. 11.
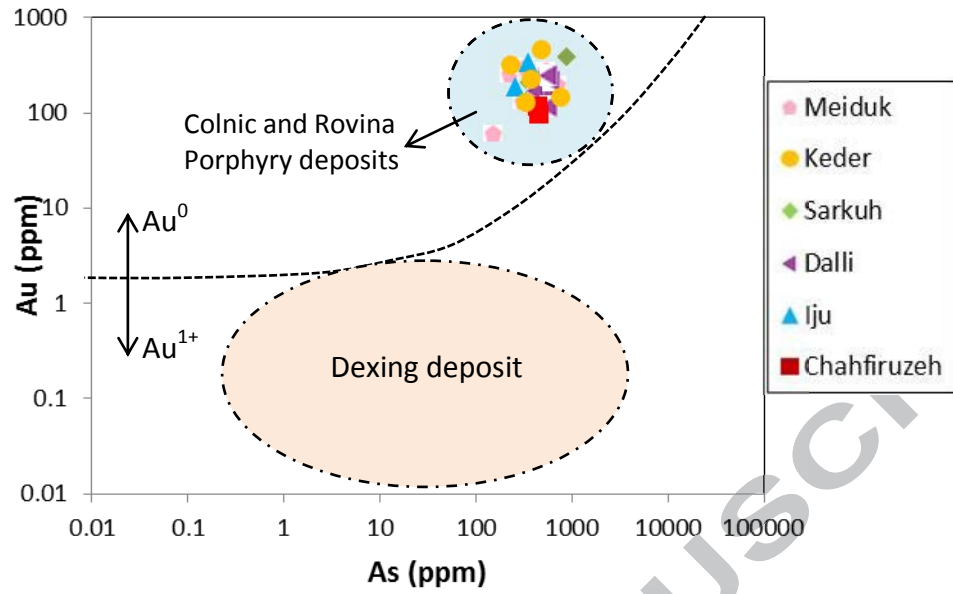
Fig. 12.
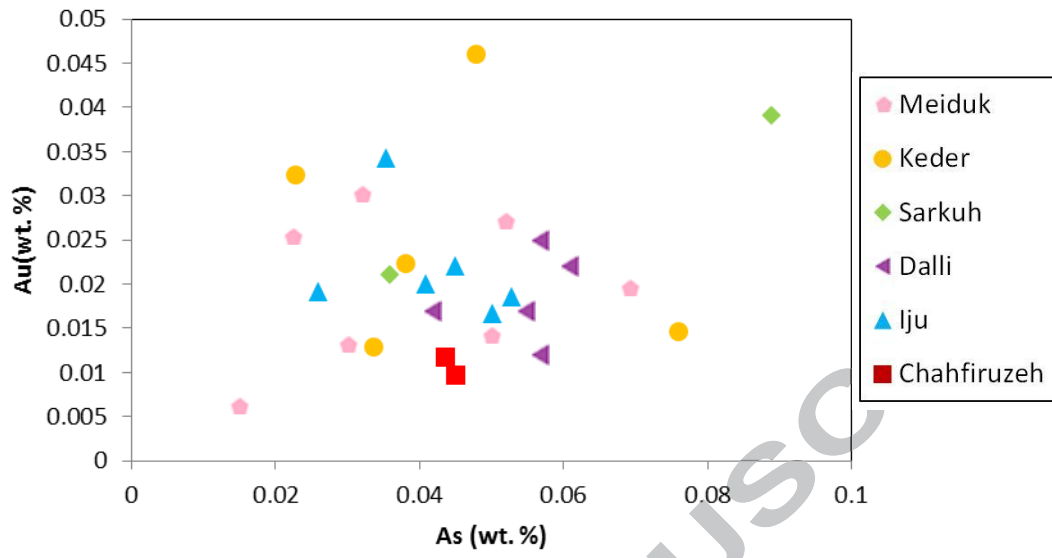
Fig. 13.
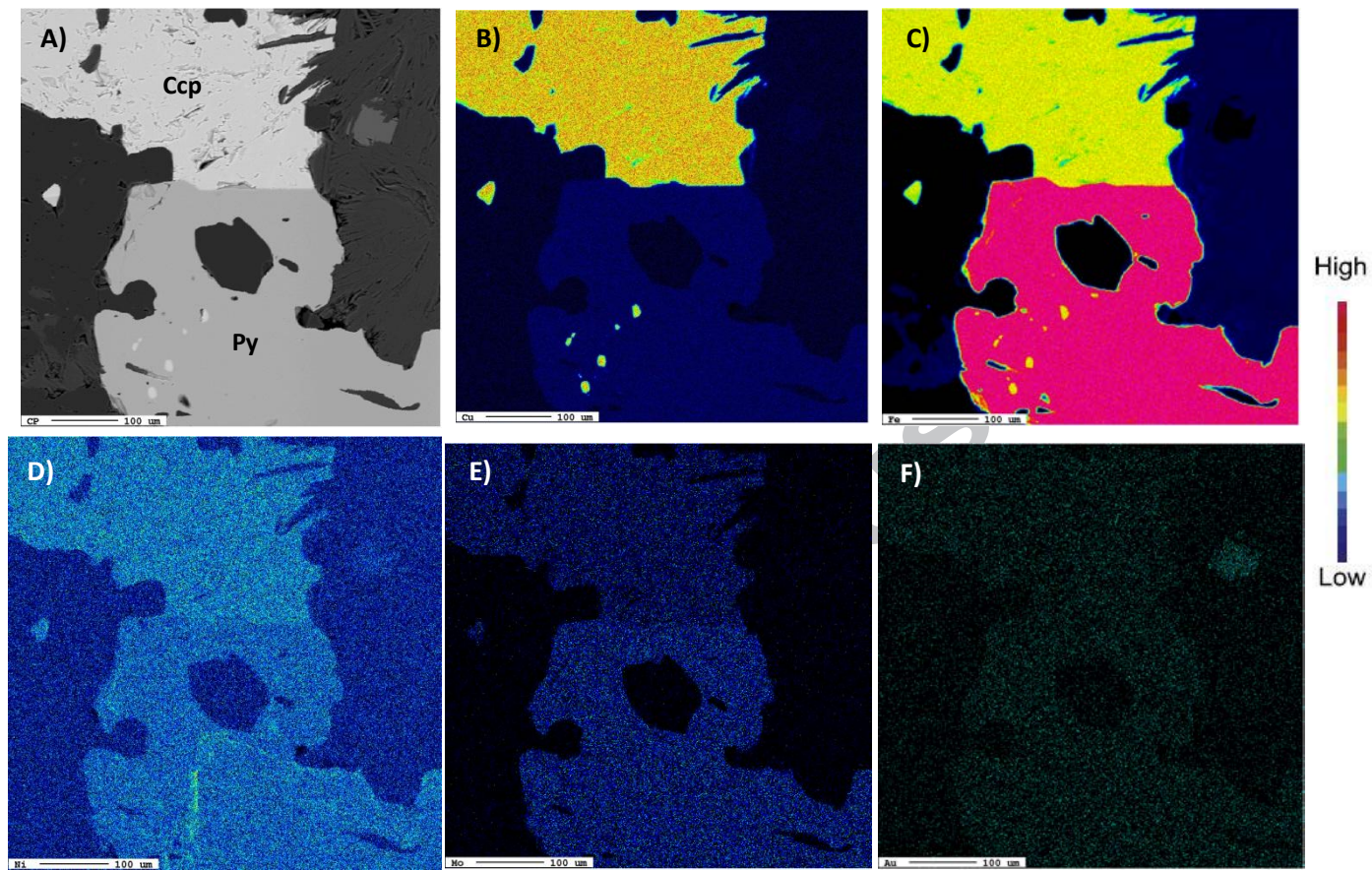
Fig. 14.
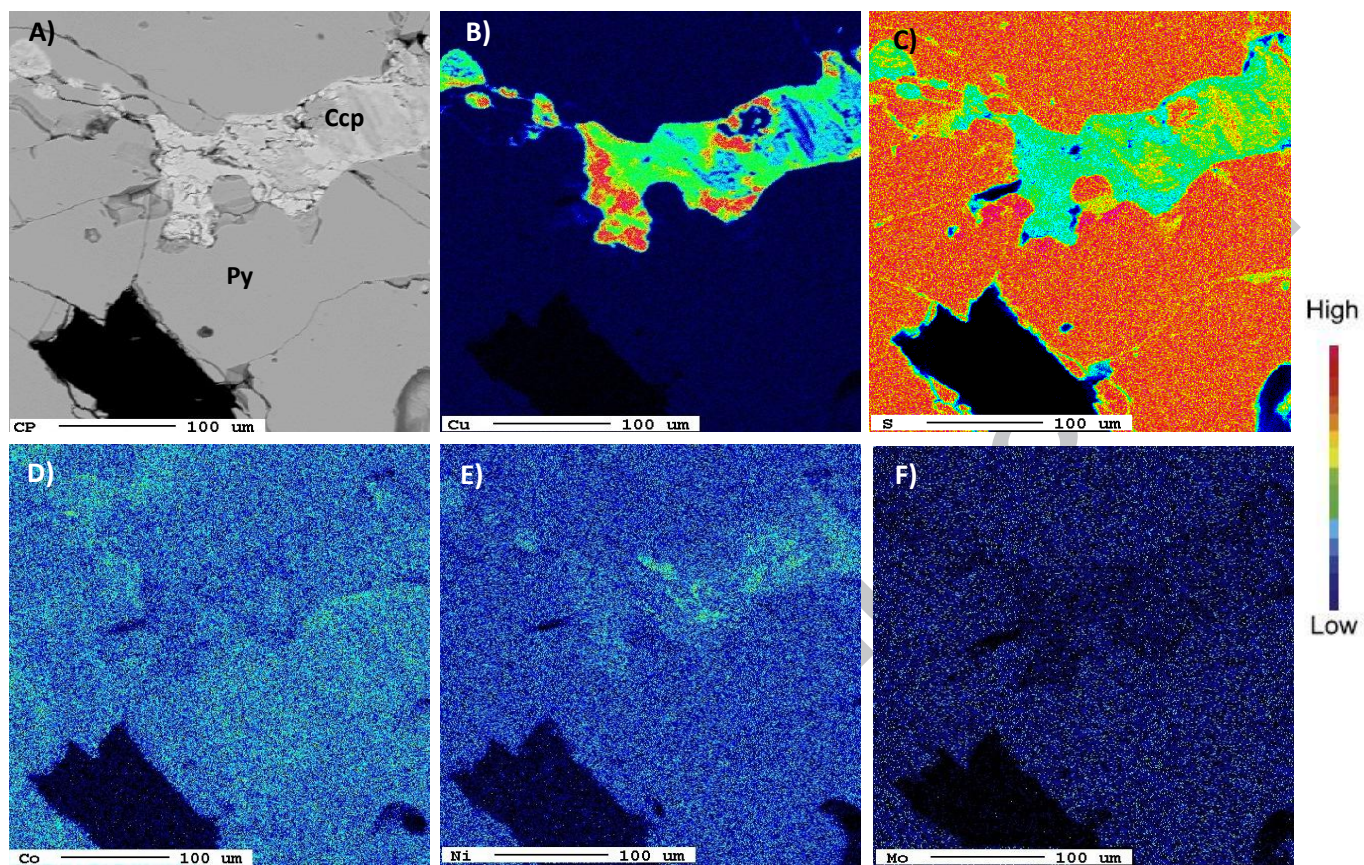
Fig. 15.

Table 1. Characteristics of selected porphyry deposits in UDMA

Porphyry	Radiometric Age	Ore-bearing Porphyry	Tonnage (Mt)	Grade
Meiduk	12.5 ± 0.5[a]	Granodiorite	170[b]	0.86% Cu[b]
Sarkuh	15.18 ± 0.43[a]	Granite, granodiorite	110[c]	0.26% Cu[c]
Iju	9.27 ± 0.5[a]	Granodiorite, tonalite	74[c]	0.31% Cu[c]
Dalli	21[d]	Diorite, quarz diorite	8[d]	0.5% Cu[d]
Chahfiruzeh	16.3 ± 0.1[e]	Quartz diorite, quartz monzodiorite	100[f]	0.4-0.8 % Cu[f]
Keder	-	Quartz diorite, diorite	-	0.06-0.16% Cu[g]

[a]McInnes et al. (2005); [b]Taghipour et al. (2008); [c]Aghazadeh et al. (2015); [d]Ayati et al. (2013); [e]Kazemi-Mehrnia, 2010; [f, g]Asadi (2013)

Table 2. Representative EMPA composition (wt%), and calculated formula for plagioclase in the selected porphyry deposits

Sample No#	MP-1	MP-2	MP-3	MP-4	MP-5	IP-1	IP-2	IP-3	IP-4	IP-5	IP-6
Sample lab. No#	MDk4-1Pl1	MDk4-1Pl2	MDk4-1Pl3	MDk4-1Pl4	MDk4-1Pl5	IjU21-2pl1	IjU21-2pl2	IjU21-2pl3	IjU21-2pl4	IjU21-2pl5	IjU21-2pl6
Porphyry	Meiduk	Meiduk	Meiduk	Meiduk	Meiduk	Iju	Iju	Iju	Iju	Iju	Iju
SiO_2	47.89	49.16	49.16	48.76	48.24	62.72	61.43	61.57	61.82	61.14	58.97
TiO_2	0.049	b.d.	0.005	0.028	0.003	0.021	b.d.	b.d.	0.013	0.015	0.026
Al_2O_3	33.11	32.52	32.07	32.68	33.09	23.86	24.57	24.43	24.80	24.47	26.17
FeO*	0.629	0.661	0.726	0.621	0.658	0.205	0.180	0.177	0.116	0.070	0.252
MnO	b.d.	0.034	b.d.	b.d.	0.030	b.d.	b.d.	b.d.	b.d.	b.d.	0.029
MgO	0.024	0.045	0.040	0.017	0.048	b.d.	b.d.	0.001	0.008	b.d.	0.013
CaO	15.78	15.27	14.98	15.34	15.85	4.81	5.88	5.90	6.02	5.39	7.58
BaO	b.d.	0.013	0.098	b.d.	0.027	0.131	b.d.	0.041	b.d.	0.049	b.d.
Na_2O	2.07	2.46	2.66	2.38	2.10	8.46	7.81	7.91	7.88	8.39	6.83
K_2O	0.073	0.085	0.110	0.081	0.070	0.570	0.408	0.435	0.431	0.490	0.309
Sum	99.64	100.25	99.86	99.92	100.12	100.80	100.30	100.49	101.10	100.03	100.20
Si	2.202	2.243	2.254	2.232	2.208	2.763	2.721	2.725	2.717	2.719	2.629
Ti	0.0016	0	0.0001	0.0009	0.0001	0.001	0.000	0.000	0.000	0.001	0.001
Al	1.795	1.749	1.733	1.763	1.785	1.239	1.283	1.274	1.285	1.283	1.375
Fe	0.024	0.025	0.027	0.023	0.025	0.008	0.007	0.007	0.004	0.003	0.009
Mn	0	0.0013	0	0	0.0011	0.000	0.000	0.000	0.000	0.000	0.001
Mg	0.0016	0.0030	0.0027	0.0011	0.0032	0.000	0.000	0.000	0.001	0.000	0.001
Ca	0.7779	0.7467	0.7362	0.7531	0.7779	0.227	0.279	0.280	0.284	0.257	0.362
Ba	0	0.0002	0.0017	0	0.0004	0.002	0.000	0.001	0.000	0.001	0.000
Na	0.1846	0.2177	0.2365	0.2120	0.1864	0.723	0.671	0.679	0.672	0.724	0.590
K	0.0042	0.0049	0.0064	0.0047	0.0040	0.032	0.023	0.025	0.024	0.028	0.018
Total cat	4.99	4.99	4.99	4.99	4.99	4.99	4.98	4.99	4.98	5.01	4.98
$CaAl_2Si_2O_8$	80.4	77.0	75.0	77.6	80.2	23.1	28.7	28.4	29.0	25.4	37.3
$BaAl_2Si_2O_8$	0	0.02	0.1	0	0.04	0.2	0.0	0.1	0.0	0.1	0.0
$NaAlSi_3O_8$	19.0	22.4	24.1	21.8	19.2	73.4	69.0	69.0	68.6	71.7	60.8

*FeO: Total iron calculated as FeO

Sample No#	SP-1	SP-2	SP-3	KP-1	KP-2	KP-3	DP-20	DP-21	DP-22	DP-23	DP-23
Sample lab. No#	SKPpa1	SKPpa2	SKPpa3	KD1-2pl1	KD1-2pl2	KD1-2pl3	S3-20	S3-21	S3-22	S3-23	S4-24
Porphyry	Sarkuh	Sarkuh	Sarkuh	Keder	Keder	Keder	Dalli	Dalli	Dalli	Dalli	Dalli
SiO_2	58.37	58.40	57.44	65.85	68.73	67.26	59.25	55.7	56.66	58.42	59.01
TiO_2	0.013	0.010	0.041	b.d.	0.008	0.038	b.d.	0.08	b.d.	0.05	0.07
Al_2O_3	25.96	26.56	27.50	19.78	19.75	19.49	26.16	28.51	27.77	26.33	24.89
FeO	0.225	0.150	0.218	0.115	0.050	0.224	b.d.	b.d.	b.d.	b.d.	b.d.
MnO	b.d.	b.d.	0.035	0.014	0.008	0.014	b.d.	b.d.	0.01	b.d.	0.02
MgO	b.d.	0.009	0.011	0.007	b.d.	0.009	b.d.	b.d.	b.d.	b.d.	0.01
CaO	7.79	8.07	9.21	0.701	0.022	0.531	7.53	10.11	9.26	7.74	6.92
BaO	0.118	0.014	0.081	b.d.	b.d.	0.206	0.16	0.1	0.05	0.04	0.11
Na_2O	6.62	6.53	6.00	9.46	11.52	8.74	7.08	5.39	5.95	6.9	6.65
K_2O	0.386	0.475	0.305	0.571	0.274	1.220	0.41	0.26	0.32	0.42	0.3
Sum	99.50	100.23	100.85	96.50	100.38	97.74	100.59	100.15	100.02	99.90	97.98
Si	2.625	2.607	2.557	2.975	2.991	3.003	2.633	2.501	2.542	2.615	2.678
Ti	0.000	0.000	0.001	0.000	0.000	0.001	0.000	0.003	0.000	0.002	0.002
Al	1.376	1.398	1.443	1.053	1.013	1.026	1.370	1.509	1.468	1.389	1.332
Fe	0.008	0.006	0.008	0.004	0.002	0.008	0.000	0.000	0.000	0.000	0.000
Mn	0.000	0.000	0.001	0.001	0.000	0.001	0.000	0.000	0.000	0.000	0.001
Mg	0.000	0.001	0.001	0.000	0.000	0.001	0.000	0.000	0.000	0.000	0.001
Ca	0.376	0.386	0.439	0.034	0.001	0.025	0.359	0.486	0.445	0.371	0.337
Ba	0.002	0.000	0.001	0.000	0.000	0.004	0.003	0.002	0.001	0.001	0.002
Na	0.578	0.566	0.518	0.829	0.972	0.757	0.610	0.469	0.518	0.599	0.585
K	0.022	0.027	0.017	0.033	0.015	0.070	0.023	0.015	0.018	0.024	0.017
Total cat	4.98	4.99	4.98	4.92	4.99	4.89	4.99	4.98	4.99	5.00	4.95
$CaAl_2Si_2O_8$	38.4	39.4	45.0	3.8	0.1	3.0	36.0	50.0	45.3	37.3	35.8
$BaAl_2Si_2O_8$	0.2	0.0	0.1	0.0	0.0	0.4	0.3	0.2	0.1	0.1	0.2

$NaAlSi_3O_8$	59.1	57.8	53.1	92.5	98.4	88.5	61.3	48.3	52.7	60.2	62.2

Table 3. Representative EMPA composition (wt%), and calculated formula for reequilibrated biotite associated with potassic alteration of selected porphyry deposits

Sample No#	CB-3	CB-5	KB-134	KB-135	SB-89	SB-90	SB-91	IB-52	IB-53	IB-54
Sample lab. No#	s1-3	s1-5	s-2-134	s-2-135	s-2-89	s-2-90	s-2-91	s-2-52	s-2-53	s-2-54
Porphyry	Chahfiruzeh	Chahfiruzeh	Keder	Keder	Sarkuh	Sarkuh	Sarkuh	Iju	Iju	Iju
SiO_2	38.82	37.31	39.26	39.95	38.42	38.44	38.71	37.67	38.73	38.34
TiO_2	4.54	4.40	4.30	4.18	3.95	4.68	3.97	4.58	4.01	4.20
Al_2O_3	13.10	12.99	12.50	12.95	14.45	14.22	14.79	14.54	17.84	14.30
FeO	12.03	12.26	10.19	10.73	14.81	14.89	14.94	16.02	11.83	13.67
MnO	0.16	0.22	0.300	0.240	0.08	0.08	0.07	0.11	0.08	0.12
MgO	17.59	18.11	16.72	18.32	15.22	15.09	15.04	15.57	13.40	15.93
CaO	0.15	0.30	0.210	0.060	b.d.	b.d.	0.03	0.10	0.05	0.03
Na_2O	0.16	0.13	0.310	0.170	0.15	0.21	0.17	0.31	0.27	0.35
K_2O	7.81	8.66	8.93	9.51	9.49	9.50	9.29	7.90	7.75	9.09
BaO	0.11	0.17	0.050	0.020	0.49	0.54	0.58	1.23	1.03	1.38
F	1.68	0.07	1.12	2.25	b.d.	0.95	0.83	1.13	1.35	1.41
Cl	0.24	0.26	0.130	0.160	0.28	0.24	0.27	0.18	0.20	0.23
Si	2.858	2.779	2.937	2.894	2.82	2.809	2.822	2.752	2.828	2.807
Al(IV)	1.137	1.14	1.063	1.106	1.18	1.191	1.178	1.248	1.172	1.193
Ti	0.251	0.246	0.242	0.228	0.218	0.257	0.218	0.252	0.22	0.231
Mn	0.01	0.014	0.019	0.015	0.005	0.005	0.004	0.007	0.005	0.007
Mg	1.931	2.011	1.865	1.978	1.665	1.644	1.635	1.696	1.459	1.738
Ca	0.012	0.024	0.017	0.005	0	0	0.002	0.008	0.004	0.002
Na	0.023	0.019	0.045	0.024	0.021	0.03	0.024	0.044	0.038	0.05
K	0.734	0.823	0.852	0.879	0.889	0.886	0.864	0.736	0.722	0.849
OH	1.579	1.951	1.718	1.465	1.965	1.751	1.775	1.716	1.663	1.645
F	0.391	0.016	0.265	0.516	0	0.22	0.191	0.261	0.312	0.327
Cl	0.03	0.033	0.016	0.020	0.035	0.03	0.033	0.022	0.025	0.029
Xph	0.609	0.627	0.609	0.628	0.54	0.536	0.529	0.543	0.486	0.567
Xan	0.064	0.050	0.165	0.114	0.211	0.193	0.218	0.132	0.231	0.189

Xpdo	0.245	0.242	0.128	0.181	0.154	0.175	0.151	0.241	0.086	0.153
Xmg	0.609	0.627	0.609	0.628	0.54	0.536	0.529	0.543	0.486	0.567
Xfe	0.277	0.275	0.266	0.247	0.37	0.365	0.381	0.367	0.427	0.335
X(OH)	0.789	0.975	0.859	0.732	0.982	0.875	0.888	0.858	0.832	0.822
X(F)	0.20	0.01	0.133	0.258	0.001	0.11	0.096	0.131	0.156	0.163
X(Cl)	0.02	0.02	0.008	0.010	0.017	0.015	0.017	0.011	0.012	0.014
Fe/(Fe+Mg)	0.28	0.28	0.255	0.247	0.353	0.356	0.358	0.366	0.331	0.325
$\log X_{Cl}/X_{OH}$	1.722	1.774	2.018	1.873	-1.751	-1.77	-1.726	-1.887	-1.827	-1.761
$\log X_F/X_{OH}$	-0.606	-2.073	-0.812	-0.453	-3.293	-0.901	-0.967	-0.818	-0.727	-0.702
$\log X_F/X_{Cl}$	1.16	-0.29	1.206	1.419	-1.542	0.869	0.759	1.069	1.1	1.059
$\log f(H_2O)f(HF)$fluid	4.119	5.606	4.35	4.013	6.883	4.487	4.544	4.378	4.221	4.29
$\log f(H_2O)/f(HCl)$fluid	3.908	3.97	4.216	4.082	3.974	3.99	3.942	4.095	4.002	3.983
$\log f(HF)/f(HCl)$fluid	-0.891	-2.335	-0.819	-0.638	-3.542	-1.125	-1.223	-0.913	-0.783	-0.965
Temperature °C	464.6	489.4	464	491	380.1	376.2	369.0	383.7	328.9	410.1

FeO: Total iron calculated as FeO. The XPh (phlogopite), Xan (annite), Xpdo (proton-deficient oxyannite), are mole fractions calculated on the basis of octahedral ions (Jacobs and Parry 1979).

Sample No#	MB-9	MB-10	MB-12	DB-19	DB-20	DB-23
Sample lab. No#	S2-9	S2-10	S2-12	s1-19	s1-20	s1-23
Porphyry	Meiduk	Meiduk	Meiduk	Dalli	Dalli	Dalli
SiO_2	38.79	38.36	40.46	38.82	38.57	38.41
TiO_2	1.90	1.96	1.98	5.25	5.64	5.15
Al_2O_3	16.04	16.49	15.97	12.93	12.22	12.88
FeO	14.16	14.16	13.18	12.06	12.41	12.07
MnO	0.07	0.08	0.11	0.25	0.25	0.23
MgO	15.05	15.69	15.51	17.05	16.39	17.40
CaO	0.28	0.25	0.15	0.03	0.21	0.30
Na_2O	0.05	0.10	0.05	0.12	0.17	0.16

K$_2$O	8.10	8.65	9.41	8.13	8.96	8.85
BaO	0.20	0.17	0.18	0.36	0.15	0.25
F	b.d.	0.21	b.d.	1.77	0.68	0.68
Cl	0.13	0.13	0.18	0.2	0.26	0.25
Si	2.869	2.812	2.916	2.855	2.859	2.821
Al(IV)	1.131	1.188	1.084	1.121	1.068	1.115
Ti	0.106	0.108	0.107	0.29	0.314	0.284
Mn	0.004	0.005	0.007	0.016	0.016	0.014
Mg	1.659	1.714	1.666	1.869	1.811	1.905
Ca	0.022	0.02	0.012	0.002	0.017	0.024
Na	0.007	0.014	0.007	0.017	0.024	0.023
K	0.764	0.809	0.865	0.763	0.847	0.829
Ba	0.006	0.005	0.005	0.01	0.004	0.007
OH	1.984	1.935	1.978	1.563	1.808	1.811
F	b.d.	0.049	b.d.	0.412	0.159	0.158
Cl	0.016	0.016	0.022	0.025	0.033	0.031
Xph	0.527	0.545	0.53	0.593	0.577	0.602
Xan	0.261	0.238	0.208	0.062	0.101	0.078
Xpdo	0.092	0.106	0.139	0.248	0.216	0.225
Xmg	0.527	0.545	0.53	0.593	0.577	0.602
Xfe	0.408	0.392	0.39	0.284	0.298	0.280
X(OH)	0.991	0.968	0.989	0.782	0.904	0.905
X(F)	0.001	0.024	0.001	0.21	0.08	0.08
X(Cl)	0.008	0.008	0.011	0.01	0.02	0.02
Fe/(Fe+Mg)	0.345	0.336	0.323	0.28	0.30	0.28
logXCl/XOH	-2.085	-2.078	-1.954	1.797	1.743	1.765
logXF/XOH	-3.297	-1.599	-3.296	-0.579	-1.054	-1.059
logXF/XCl	-1.212	0.479	-1.342	1.21	0.68	0.70
log$f$(H$_2$O)f(HF)fluid	7.682	6.009	7.684	4.075	4.532	4.565
log$f$(H$_2$O)/f(HCl)fluid	4.695	4.702	4.566	3.974	3.911	3.947
Temperature ºC	367.1	385.6	369.7	442.7	423.0	455.1

45

Table 4. Representative EMPA analyses of pyrite (wt. %) associated with potassic alteration of porphyry deposits.

Sample No#	MPY-8	MPY-9	IPY-1	IPY-2	SPY-2	SPY-3	DPY-4	DPY-3	CPY-1	CPY-2	KPY-4	KPY-5
Sample lab. No#	MDK-10-2py2	MDK-10-1py1	IJU-21p1	IJU-21p2	SKP-2py1	SKP-2py2	dh6gam2	DH2NFS-8-1py2	CHF-6-3p1	CHF-6-3p2	K13p1	K13p2
Porphyry	Meiduk	Meiduk	Iju	Iju	Sarkuh	Sarkuh	Dalli	Dalli	Chahfiruzeh	Chahfiruzeh	Keder	Keder
As	0.032	0.015	0.035	0.050	0.036	0.089	0.057	0.042	0.045	0.043	0.022	0.038
Te	b.d.	0.003	0.0008	0.016	0.005	b.d.	0.003	b.d.	b.d.	b.d.	0.002	0.008
S	51.13	52.42	52.01	52.16	53.29	52.46	52.27	51.57	51.74	52.20	52.47	52.04
Fe	45.64	46.47	46.73	46.73	46.41	46.51	45.20	46.53	46.24	46.43	46.35	46.61
Cu	1.357	0.034	0.014	0.001	0.013	b.d.	0.015	0.118	0.0003	b.d.	b.d.	b.d.
Se	b.d.	b.d.	b.d.	0.006	b.d.	b.d.	b.d.	b.d.	b.d.	b.d.	b.d.	b.d.
Bi	b.d.	0.001	b.d.	b.d.	b.d.	b.d.	b.d.	b.d.	b.d.	b.d.	b.d.	b.d.
Re	b.d.	b.d.	0.004	0.005	b.d.	0.003	0.007	b.d.	b.d.	b.d.	b.d.	0.011
Ni	b.d.	0.023	b.d.	b.d.	b.d.	b.d.	b.d.	b.d.	0.021	0.027	b.d.	0.018
Co	0.084	0.127	0.090	0.090	0.086	0.142	0.065	0.077	0.085	0.084	0.101	0.094
Ge	b.d.	b.d.	b.d.	b.d.	b.d.	b.d.	b.d.	b.d.	b.d.	b.d.	b.d.	b.d.
Hg	b.d.	b.d.	b.d.	b.d.	b.d.	b.d.	b.d.	b.d.	b.d.	b.d.	b.d.	b.d.
Au	0.030	0.006	0.034	0.016	b.d.	0.039	0.012	0.017	0.009	0.011	0.032	0.022
Zn	b.d.	b.d.	b.d.	0.001	b.d.	b.d.	b.d.	b.d.	b.d.	0.0001	0.020	b.d.
Th	b.d.	b.d.	b.d.	b.d.	0.005	b.d.	b.d.	0.006	b.d.	b.d.	b.d.	b.d.
Sb	b.d.	b.d.	b.d.	b.d.	0.008	b.d.	b.d.	b.d.	0.018	0.010	b.d.	b.d.
Ag	b.d.	b.d.	0.0003	b.d.	b.d.	b.d.	0.002	b.d.	0.006	b.d.	b.d.	b.d.
Pb	b.d.	b.d.	b.d.	b.d.	b.d.	b.d.	b.d.	b.d.	b.d.	b.d.	b.d.	b.d.
Mo	0.680	0.676	0.710	0.695	0.686	0.686	0.684	0.684	0.716	0.707	0.706	0.705
Total	98.96	99.77	99.63	99.77	100.55	99.93	98.32	99.05	98.88	99.51	99.70	99.54

Table 5. Representative EMPA analyses of chalcopyrite (wt. %) associated with potassic alteration of porphyry deposits

Sample No#	MCP-1	MCP-2	ICP-1	ICP-2	SCP-1	SCP-2	DCP-1	DCP-2	CCP-1	CCP-2	KCP-1
Sample lab. No#	MDk84cp1	MDk84cp2	IJU-21cp	IJU-21cp	SKP-2cp1	SKP-2cp2	dh6gam6cpy-1	dh6gam7cpy-2	CHF-chp2	CHFchp10	KDR11-3cp1
Porphyry	Meiduk	Meiduk	Iju	Iju	Sarkuh	Sarkuh	Dalli	Dalli	Chahfiruzeh	Chahfiruzeh	Keder
As	0.057	0.044	0.057	0.047	b.d.	0.033	0.009	0.042	0.038	0.035	0.030
Te	0.005	b.d.	0.008	0.005	0.012	0.006	b.d.	0.003	b.d.	b.d.	b.d.
S	34.56	34.25	33.94	34.25	34.29	34.24	34.92	35.38	35.18	34.73	34.51
Fe	30.29	30.41	30.35	30.12	30.55	30.43	29.77	29.80	29.97	30.02	27.99
Cu	34.23	34.30	34.18	34.15	34.15	34.18	33.36	33.70	34.02	33.72	36.49
Se	b.d.	b.d.	b.d.	b.d.	b.d.	b.d.	b.d.	b.d.	b.d.	b.d.	b.d.
Bi	b.d.	b.d.	b.d.	b.d.	b.d.	b.d.	b.d.	b.d.	b.d.	b.d.	b.d.
Re	b.d.	b.d.	0.002	b.d.	b.d.	0.015	b.d.	b.d.	b.d.	b.d.	0.010
Ni	b.d.	b.d.	b.d.	b.d.	b.d.	b.d.	b.d.	b.d.	b.d.	b.d.	b.d.
Co	0.057	0.053	0.053	0.063	0.044	0.046	0.043	0.041	0.041	0.048	0.049
Ge	b.d.	b.d.	b.d.	b.d.	b.d.	b.d.	b.d.	b.d.	b.d.	b.d.	b.d.
Hg	0.0008	0.029	b.d.	0.034	0.004	b.d.	b.d.	b.d.	b.d.	b.d.	b.d.
Au	0.005	b.d.	b.d.	b.d.	0.017	b.d.	0.015	0.010	b.d.	0.001	0.021
Zn	0.098	0.080	0.086	0.079	0.064	0.071	0.041	0.049	0.072	0.070	0.065
Th	b.d.	b.d.	b.d.	0.005	0.003	0.005	0.002	0.008	0.002	b.d.	b.d.
Sb	b.d.	0.007	b.d.	0.008	0.003	b.d.	b.d.	b.d.	b.d.	b.d.	b.d.
Ag	0.006	b.d.	b.d.	b.d.	b.d.	0.011	b.d.	0.006	b.d.	b.d.	b.d.
Pb	0.003	b.d.	b.d.	b.d.	b.d.	0.004	b.d.	b.d.	0.014	0.007	0.020
Mo	0.529	0.519	0.509	0.513	0.498	0.493	0.508	0.500	0.490	0.486	0.5143
Total	99.84	99.69	99.18	99.27	99.65	99.53	98.68	99.55	99.83	99.13	99.70